

Dynamics of the rotated Dicke model

Michael Tomka[✉] and Vladimir Gritsev[✉]

[✉]*Physics Department, University of Fribourg, Chemin du Musée 3, 1700 Fribourg, Switzerland*

(Dated: August 14, 2021)

We study quantum dynamics of the rotationally driven Dicke model where the collective spin is rotated around the z axis with a finite velocity. In the absence of the rotating wave approximation we observe that for several physically relevant initial states the position of the quantum critical point is shifted by the amount given by the applied rotation velocity. This allows us to probe the quantum criticality “from a distance” in parameter space without actual crossing of the quantum critical surface but instead by encircling it in the parameter space. This may provide a useful experimental hint since the quantum state is not destroyed by this protocol. Moreover, for the coherent initial state we observe an interesting non-equilibrium reentrant phenomenon of quantum critical behavior as a function of the driving velocity and construct a non-equilibrium phase diagram of the driven model.

PACS numbers:

I. INTRODUCTION

The Dicke model [1], [2] was introduced to model the interaction of a collection of N two-level atoms with a single-mode radiation (bosonic) field through the dipole coupling. Under the condition that the ensemble of two-level atoms is confined in a region of space which is much smaller than the wavelength of the single-mode radiation field, the system of the two-level emitters behaves as a collective large spin. The model became a paradigm for collective behavior of matter interacting with light and is believed to have a phase transition at finite and zero temperatures [3], [4], [5]. A super-radiant transition is characterized by the expectation value of the photon number operator which distinguishes between normal phase (where it is zero) and a super-radiant phase (where it is nonzero). The issue of this phase transition has been debated [6] in length in the literature by various authors using different methods. The conclusion is that although it is difficult to realize the phase transition in a real two-level system for which the model has been introduced, it is possible to engineer it in some cavity QED setups. For a recent review of these issues see, e.g., [7], [8].

With a recent progress in quantum optics and cold atoms it became possible to realize the Dicke model in a cavity QED systems and observe a super-radiant phase transition and other collective behaviors [9]. This advance became possible by achieving considerable degree of tuneability of parameters of the system with high precision. Moreover parameters can be controlled in real time. This stimulates studies of non-equilibrium effects in this class of systems. An interplay between collective and non-equilibrium effects is pronounced close to the quantum phase transition. Several recent theoretical works on driven non-equilibrium Dicke model, [10], [11], [12] and [13] have focused on various effects of time-depending driving of the interaction strength and/or detuning. Many of these non-equilibrium effects are related to the presence of a quantum critical point in the equilibrium model.

Here we propose to probe the quantum phase transition appearing in the Dicke model in an indirect way. We employ a certain degree of tuneability of the system to drive (rotate) the collective spin by a certain time-dependent angle. This makes it possible to probe the quantum criticality “from a distance” in parameter space without crossing the equilibrium quantum critical point. Apart from this we observe new, reentrant quantum critical behavior in such non-equilibrium protocol for certain initial state. This behavior can be traced back to a mechanism of competition between geometric and dynamical phases in the non-equilibrium dynamics [14].

In addition to the previous studies, here we look into the quantum dynamics of the rotationally driven Dicke model when the change of the rotation angle is linear in time. We distinguish between two types of protocols (see Fig. 1): in one case we encircle the critical surface in the parameter space from the outer region (contour \mathcal{C}_1) while in the second case we drive the system in such a way that the circle \mathcal{C}_2 stays inside the region bounded by the critical surface. These regions are distinguished by the presence (region \mathcal{C}_1) or absence (region \mathcal{C}_2) of the geometric phase contributions to the total phase factor of each instantaneous eigenstate. To characterize the non-equilibrium phase diagram we look into two types of observables: (i) the mean photon number and (ii) a topological number associated with the expectation value of the parity operator.

Moreover we consider several different initial states: (i) atom-field coherent states (coherent state for photons and pseudo-spin subsystem), (ii) Fock state and (iii) the ground state of the system. Our quasi-classical approach which is based on the coherent state representation is supplemented by a numerical procedure. For initial coherent and ground states a non-equilibrium phase diagram has an additional reentrant phase inside the super-radiant phase. For the aims of completeness and comparison with a driven system, we also look into dynamics of the undriven Dicke model starting from those initial states. We study the system both for a finite num-

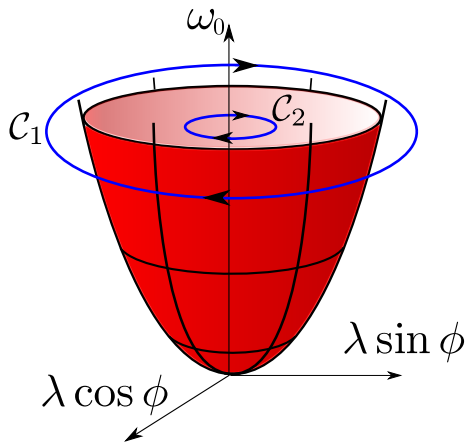


Figure 1: Equilibrium quantum phase diagram of the rotationally driven Dicke model as a function of atomic frequency ω_0 and atom-photon coupling strength λ . Paths C_1 and C_2 are fixed by the time dependence of the driving parameter $\phi(t)$ (rotation angle around z -direction in spin space). Here the bosonic frequency is set to $\omega = 1$.

ber of two-level systems and in the thermodynamic limit (TDL). We found in particular that dynamics starting from the coherent state coincides with the one for the initial ground state, both in the driven and undriven cases. Dynamics from the pure Fock state is featureless in the thermodynamic limit: one needs some fluctuations in the initial state to make it evolve, at least in the quasi-classical approach. These fluctuations are introduced by allowing small fluctuations in the bosonic and the spin sectors; we call it “nearly-Fock” state. Our results for the non-equilibrium phase diagram of the driven Dicke model are summarized in Fig. 8.

We note that here we study the Dicke model beyond the rotating wave approximation which means that it is not integrable. Dynamics of an integrable variant of the Dicke model starting from certain initial states (when the rotating wave approximation is made) has been studied before in [15] and more recently in [16], [17]. We however found some features (like e.g. formation of soliton-like trains in the thermodynamic limit) which also hold in the non-integrable case.

First, we overview some basic facts about the Dicke model (Section II), while in Section III we establish quasi-classical equations for the dynamically driven model. Section IV presents various results for several initial conditions and compares the dynamics of the driven and undriven models.

II. THE DICKE MODEL

Here we consider the Dicke model without the rotating wave approximation. The quantum Hamiltonian of the

Dicke model reads

$$\hat{H}_D = \omega_0 \hat{J}_z + \omega \hat{a}^\dagger \hat{a} + \frac{\lambda}{\sqrt{N}} (\hat{a}^\dagger + \hat{a}) (\hat{J}_+ + \hat{J}_-), \quad (1)$$

where ω_0 is the level-splitting of a two-level atom and the collection of those N identical two-level atoms is described by the collective spin operators $\hat{J}_\mu = \sum_{i=1}^N \hat{\sigma}_i^\mu / 2$. Here $\hat{\sigma}_i^\mu$, $\mu = z, \pm$ are the usual Pauli matrices which describe a two-level emitter. The collective spin operators satisfy the $\mathfrak{su}(2)$ Lie algebra:

$$[\hat{J}_+, \hat{J}_-] = 2\hat{J}_z, \quad [\hat{J}_z, \hat{J}_\pm] = \pm \hat{J}_\pm. \quad (2)$$

The Hilbert space of the $\mathfrak{su}(2)$ Lie algebra is spanned by the Dicke states $|j, m\rangle$, with $m = -j, -j+1, \dots, j-1, j$ and j being integer or half integer. The Dicke states $|j, m\rangle$ are the eigenstates of \hat{J}^2 and \hat{J}_z with eigenvalues $j(j+1)$ and m , respectively. As in [18] we fix j to its maximal value $j = N/2$. Therefore the collection of two-level atoms can be interpreted as a large “spin” (pseudo-spin) vector of magnitude $j = N/2$. The single-mode radiation field with frequency ω is described by the bosonic creation and annihilation operators \hat{a}, \hat{a}^\dagger satisfying the usual commutation relation $[\hat{a}, \hat{a}^\dagger] = \hat{1}$. The set of operators $\{\hat{a}^\dagger \hat{a}, \hat{a}^\dagger, \hat{a}, \hat{1}\}$ forms the Heisenberg-Weyl Lie algebra \mathfrak{h}_4 . The Hilbert space of this algebra is spanned by the Fock states $|n\rangle$ with $n = 0, 1, 2, 3, \dots$, defined by

$$\hat{a}^\dagger |n\rangle = \sqrt{n+1} |n+1\rangle, \quad \hat{a} |n\rangle = \sqrt{n} |n-1\rangle. \quad (3)$$

Finally, the term $\frac{\lambda}{\sqrt{N}} (\hat{a}^\dagger + \hat{a}) (\hat{J}_+ + \hat{J}_-)$ describes the atom-field interaction within the dipole approximation where the coupling strength is λ and the factor $\frac{1}{\sqrt{N}}$ stems from the fact that the original dipole coupling strength is proportional to $\frac{1}{\sqrt{V}}$.

The symmetries of the Dicke model are found by applying a unitary transformation of the form

$$\hat{U}(\varphi_0) = \exp [i\varphi_0 \hat{N}], \quad (4)$$

to the Dicke Hamiltonian \hat{H}_D . Here $\hat{N} = \hat{a}^\dagger \hat{a} + \hat{J}_z + j$ is the excitation number operator, the operator which counts the number of excited quanta in the system and φ_0 is some rotation angle. Applying this transformation we observe that

$$\hat{U} \hat{a} \hat{U}^\dagger = e^{i\varphi_0} \hat{a}, \quad \hat{U} \hat{J}_+ \hat{U}^\dagger = e^{i\varphi_0} \hat{J}_+, \quad (5)$$

and therefore, the transformed Dicke Hamiltonian reads

$$\begin{aligned} \hat{U} \hat{H}_D \hat{U}^\dagger &= \omega_0 \hat{J}_z + \omega \hat{a}^\dagger \hat{a} \\ &+ \frac{\lambda}{\sqrt{2j}} \left(\hat{a}^\dagger \hat{J}_+ e^{2i\varphi_0} + \hat{a}^\dagger \hat{J}_- + \hat{a} \hat{J}_+ + \hat{a} \hat{J}_- e^{-2i\varphi_0} \right). \end{aligned} \quad (6)$$

The Dicke model remains invariant under this transformation only if $\varphi_0 = \pi$. Hence, the associated symmetry of the Dicke model without the rotating wave approximation is the parity, since

$$\hat{U}(\varphi_0 = \pi) = \exp [i\pi \hat{N}] =: \hat{\Pi}. \quad (7)$$

This has the interpretation as a \mathbb{Z}_2 symmetry because it has the eigenvalues $e^{i\pi(n+m+j)} = \pm 1$. Thus the Hilbert space breaks up into two non-interacting subspaces, one with an even excitation number $n + m + j$ and one with an odd one. Therefore, the Dicke model without the rotating wave approximation possesses a \mathbb{Z}_2 symmetry.

The Dicke model (1) has a quantum phase transition in the thermodynamic limit $N \rightarrow \infty$ ($j \rightarrow \infty$) at the quantum critical point $\lambda_c = \frac{\sqrt{\omega\omega_0}}{2}$. Quantum critical points (criticalities) are points in the underlying parameter space $(\omega_0, \omega, \lambda)$ at which the excitation energy vanishes. Hence, the ground state of the system changes qualitatively from a normal to a super-radiant one. In the super-radiant phase the ground state is a macroscopically excited collective state that possesses the potential to super-radiate. A phase transition is associated to spontaneous breakdown of the \mathbb{Z}_2 symmetry described above. The super-radiant emission is a collective effect involving all the N two-level atoms in the sample. In this case the decay rate is $\Gamma \sim N^2\gamma_0$ instead of $N\gamma_0$, the rate for independent atom emission. Here γ_0 is the decay rate of an excited two-level atom.

In this paper we study a rotationally driven version of the Dicke model [19], [20], which results from applying a rotation of angle ϕ around the z axis to each two-level atom. Explicitly it has the form of time-dependent unitary rotation applied to z axis,

$$\hat{R}_z(t) = \exp \left[-i\phi(t)\hat{J}_z \right]. \quad (8)$$

The resulting time dependent Hamiltonian $\hat{H}_{RD}(t) = \hat{R}_z^\dagger(t)\hat{H}_D(\omega_0, \omega, \lambda)\hat{R}_z(t)$ reads

$$\begin{aligned} \hat{H}_{RD}(t) = & \omega_0\hat{J}_z + \omega\hat{a}^\dagger\hat{a} + \\ & + \frac{\lambda}{\sqrt{2j}} (\hat{a}^\dagger + \hat{a}) \left(e^{i\phi(t)}\hat{J}_+ + e^{-i\phi(t)}\hat{J}_- \right). \end{aligned} \quad (9)$$

Hence, the applied time dependent rotation $\hat{R}_z^\dagger(t)$ can be interpreted as a rotation of the pseudo-spin vector $\hat{\mathbf{J}}$ of length $j = N/2$ around the z axis by an angle $\phi(t)$.

Since the rotated Dicke Hamiltonian $\hat{H}_{RD}(t)$ is obtained by applying a unitary transformation, namely by the rotation $\hat{R}_z(t)$, the eigenvalues (eigenenergies) of the rotated Hamiltonian remain the same. Therefore, the quantum criticalities of the rotated Dicke Hamiltonian can be obtained by applying a rotation around the z axis to the time independent Dicke Hamiltonian. We use this fact and the results of Ref. [18] where the time independent Dicke Hamiltonian is diagonalized in the thermodynamic limit. In the ‘‘normal’’ phase (NP) the excitation energy reads

$$\epsilon_-^{(NP)} = \sqrt{\frac{1}{2} \left(\omega^2 + \omega_0^2 - \sqrt{(\omega_0^2 - \omega^2)^2 + 16\lambda^2\omega\omega_0} \right)}, \quad (10)$$

in which the reality condition $\lambda \leq \frac{\sqrt{\omega\omega_0}}{2}$ needs to be fulfilled. Similarly, in the ‘‘super-radiant’’ phase (SRP)

the excitation energy is

$$\epsilon_-^{(SRP)} = \frac{1}{\sqrt{2}} \left(\frac{16\lambda^4}{\omega^2} + \omega^2 - \sqrt{f(\omega, \lambda)} \right)^{\frac{1}{2}}, \quad (11)$$

which is real under the condition that $\lambda \geq \frac{\sqrt{\omega\omega_0}}{2}$, where $f(\omega, \lambda) = \left(\frac{16\lambda^4}{\omega^2} - \omega^2 \right)^2 + 4\omega^2\omega_0^2$. Hence, the critical coupling at which the quantum phase transition occurs is given by $\lambda_c = \frac{\sqrt{\omega\omega_0}}{2}$. Using this relation we plot the equilibrium phase diagram for $\omega = 1$. We parametrize it by $\lambda \cos \phi$ for the x axis, and $\lambda \sin \phi$ for the y axis and ω_0 on the z axis. This is shown in Fig. 1 for the purpose of illustration of our setup.

III. COHERENT STATE REPRESENTATION - CLASSICAL ANALOGUE - TIME DEPENDENT MEAN FIELD THEORY

For concreteness of our protocol we will study quantum dynamics governed by the Hamiltonian (9) when $\phi(t)$ is linear in time

$$\phi(t) = \delta_\phi t, \quad (12)$$

where δ_ϕ is the driving velocity and the time interval is $0 < t < t_f$. This driving protocol generates circular paths in parameter space (see Fig. 1). For $t_f = 2\pi/\delta_\phi$ the path corresponds to one closed circle. First we will be interested in the mean photon number $\langle \hat{a}^\dagger \hat{a} \rangle$ for the closed circular paths \mathcal{C}_1 and \mathcal{C}_2

$$\langle \hat{a}^\dagger \hat{a} \rangle = \langle \psi(t_f) | \hat{a}^\dagger \hat{a} | \psi(t_f) \rangle, \quad (13)$$

and for different initial quantum states $|\psi(0)\rangle$. Time evolution is governed by the time dependent Schrödinger equation $i\partial_t |\psi(t)\rangle = \hat{H}_{RD}(t) |\psi(t)\rangle$. Unfortunately, the Hamiltonian (9) $\hat{H}_{RD}(t)$ is not a linear function of the generators of the dynamical group, here $SU(2)$ and H_4 . Therefore, an exact solution of the time dependent Schrödinger equation is difficult to obtain and we have to rely on some approximate methods which may become exact in certain limits (e.g. in the thermodynamic limit of $j \rightarrow \infty$). For this reason we will be interested in the dynamics in the large spin limit ($j \rightarrow \infty$) and also since the actual quantum phase transition only occurs in the thermodynamic limit. In this respect the use of the basis of coherent states is optimal because of the semi-classical nature of this basis. Further, the use of the coherent states allows us to write some time dependent mean field approximation for the dynamics which in the thermodynamic limit (semi-classical limit) becomes exact. In particular, the spin coherent states [21] ($SU(2)$ coherent states) are defined as

$$|\zeta(t)\rangle = \frac{1}{(1 + \zeta(t)\zeta(t)^*)^j} \exp \left(\zeta(t)\hat{J}_+ \right) |j, -j\rangle \quad (14)$$

where $|j, -j\rangle$ is the lowest eigenstate of \hat{J}_z , $\hat{J}_z|j, -j\rangle = -j|j, -j\rangle$. The parameter $\zeta(t) \in \mathbb{C}$ results from the parametrization of the two-dimensional sphere S^2 by the stereographic projection

$$\zeta = \tan \frac{\theta}{2} e^{i\varphi}. \quad (15)$$

Matrix elements of the spin operators in this basis are given by

$$\langle \zeta | \hat{J}_+ | \zeta \rangle = 2j \frac{\zeta^*}{1 + \zeta \zeta^*}, \quad (16)$$

$$\langle \zeta | \hat{J}_- | \zeta \rangle = \left(\langle \zeta | \hat{J}_+ | \zeta \rangle \right)^*, \quad (17)$$

$$\langle \zeta | \hat{J}_z | \zeta \rangle = \zeta \langle \zeta | \hat{J}_+ | \zeta \rangle - j = -j \frac{1 - \zeta \zeta^*}{1 + \zeta \zeta^*}. \quad (18)$$

Similarly, for the bosonic part of the system we have [21]

$$|\alpha(t)\rangle = \exp\left(-\frac{1}{2}\alpha(t)\alpha^*(t)\right) \exp(\alpha(t)\hat{a}^\dagger) |0\rangle, \quad (19)$$

where $|0\rangle$ is the field vacuum state $\hat{a}|0\rangle = 0$ and $\alpha(t) \in \mathbb{C}$ a complex number. It is also convenient to introduce the following parametrization

$$\zeta(t) = \frac{q_1(t) + ip_1(t)}{\sqrt{4j - (q_1^2(t) + p_1^2(t))}}, \quad (20)$$

$$\alpha(t) = \frac{1}{\sqrt{2}}(q_2(t) + ip_2(t)), \quad (21)$$

where (q_1, p_1, q_2, p_2) describe the phase space of the system under consideration and the indices 1 and 2 label the spin and the field subsystem, respectively.

Following the standard procedure of [21], [22] we can obtain time dependent mean field equations of motions. Namely, defining the classical Hamiltonian as

$$\begin{aligned} \langle \alpha | \langle \zeta | \hat{H}_{\text{RD}}(t) | \zeta \rangle | \alpha \rangle &\equiv \mathcal{H}_{\text{cl}}(t) \\ &= \frac{1}{2}\omega_0 (q_1^2 + p_1^2 - 2j) + \frac{1}{2}\omega (q_2^2 + p_2^2) + \\ &+ 2\lambda \sqrt{\frac{4j - (q_1^2 + p_1^2)}{4j}} (q_1 \cos \phi(t) + p_1 \sin \phi(t)) q_2. \end{aligned} \quad (22)$$

we consider a minimization problem for the action integral given by

$$\mathcal{S} = \int_{t_i}^{t_f} \mathcal{L}(q_1, \dot{q}_1, q_2, \dot{q}_2, t) dt, \quad (23)$$

where the corresponding Lagrangian is given by

$$\mathcal{L}(q_1, \dot{q}_1, q_2, \dot{q}_2, t) = \langle \alpha | \langle \zeta | i\partial_t - \hat{H}_{\text{RD}} | \zeta \rangle | \alpha \rangle. \quad (24)$$

The minimization leads to the Euler-Lagrange equations of motions

$$\frac{d}{dt} \left(\frac{\partial \mathcal{L}}{\partial \dot{q}_i} \right) - \frac{\partial \mathcal{L}}{\partial q_i} = 0, \quad (25)$$

from which we obtain the Hamiltonian equations of motion $\frac{\partial \mathcal{H}_{\text{cl}}}{\partial q_i} = -\dot{p}_i$ and $\frac{\partial \mathcal{H}_{\text{cl}}}{\partial p_i} = \dot{q}_i$ taking the following form

$$\begin{aligned} \dot{q}_1 &= \omega_0 p_1 - 2\lambda \frac{(\cos \phi(t) q_1 + \sin \phi(t) p_1) p_1 q_2}{\sqrt{4j(4j - (q_1^2 + p_1^2))}} + \\ &+ 2\lambda \sqrt{\frac{4j - (q_1^2 + p_1^2)}{4j}} \sin \phi(t) q_2, \end{aligned} \quad (26)$$

$$\begin{aligned} \dot{p}_1 &= -\omega_0 q_1 + 2\lambda \frac{q_1 (\cos \phi(t) q_1 + \sin \phi(t) p_1) q_2}{\sqrt{4j(4j - (q_1^2 + p_1^2))}} + \\ &- 2\lambda \sqrt{\frac{4j - (q_1^2 + p_1^2)}{4j}} \cos \phi(t) q_2, \end{aligned} \quad (27)$$

$$\dot{q}_2 = \omega p_2, \quad (28)$$

$$\dot{p}_2 = -\omega q_2 - 2\lambda \sqrt{\frac{4j - (q_1^2 + p_1^2)}{4j}} (\cos \phi(t) q_1 + \sin \phi(t) p_1). \quad (29)$$

First, let us determine the fixed points of these equations of motions in the classical phase space (q_1, p_1, q_2, p_2) . Since, these equations are explicitly time dependent we need to apply a canonical transformation $(q_1, p_1, q_2, p_2) \rightarrow (Q_1, P_1, q_2, p_2)$ that removes the explicit time dependence and then find out the fixed points. The first and the simplest fixed point is

$$q_{1,c_1} = 0, p_{1,c_1} = 0, q_{2,c_1} = 0, p_{2,c_1} = 0. \quad (30)$$

This fixed point is only stable if

$$\lambda < \frac{\sqrt{\omega(\omega_0 + \delta_\phi)}}{2}. \quad (31)$$

In addition, there are two fixed ‘‘circles’’ given by

$$q_{1,c_2} = -\sqrt{2j \left(1 - \frac{\omega(\omega_0 + \delta_\phi)}{4\lambda^2} \right)} \cos \phi(t), \quad (32)$$

$$p_{1,c_2} = -\sqrt{2j \left(1 - \frac{\omega(\omega_0 + \delta_\phi)}{4\lambda^2} \right)} \sin \phi(t), \quad (33)$$

$$q_{2,c_2} = \frac{2\lambda}{\omega} \sqrt{j \left(1 - \left(\frac{\omega(\omega_0 + \delta_\phi)}{4\lambda^2} \right)^2 \right)}, \quad (34)$$

$$p_{2,c_2} = 0, \quad (35)$$

and

$$q_{1,c_3} = \sqrt{2j \left(1 - \frac{\omega(\omega_0 + \delta_\phi)}{4\lambda^2} \right)} \cos \phi(t), \quad (36)$$

$$p_{1,c_3} = \sqrt{2j \left(1 - \frac{\omega(\omega_0 + \delta_\phi)}{4\lambda^2} \right)} \sin \phi(t), \quad (37)$$

$$q_{2,c_3} = -\frac{2\lambda}{\omega} \sqrt{j \left(1 - \left(\frac{\omega(\omega_0 + \delta_\phi)}{4\lambda^2} \right)^2 \right)}, \quad (38)$$

$$p_{2,c_3} = 0, \quad (39)$$

which are only real and stable if

$$\lambda > \frac{\sqrt{\omega(\omega_0 + \delta_\phi)}}{2}. \quad (40)$$

We plot the phase portrait of the system in Fig. 2.

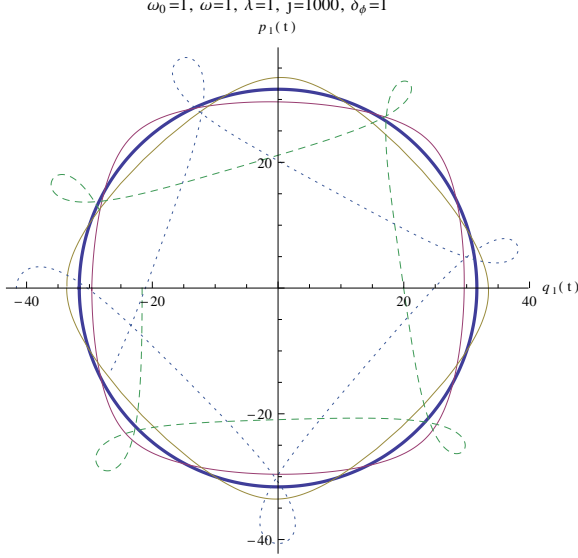


Figure 2: Plot of the phase portrait $(q_1(t), p_1(t))$ for different initial conditions.

It is instructive to note that the classical equations above can also be derived following a different procedure. Using the approach of Ref. [18] one can introduce a Holstein-Primakoff representation for the spin variables as

$$\hat{J}_+ = \hat{b}^\dagger \sqrt{2j} \sqrt{1 - \frac{1}{2j} \hat{b}^\dagger \hat{b}}, \quad (41)$$

$$\hat{J}_- = \sqrt{2j} \sqrt{1 - \frac{1}{2j} \hat{b}^\dagger \hat{b}} \hat{b}, \quad (42)$$

$$\hat{J}_z = \hat{b}^\dagger \hat{b} - j. \quad (43)$$

Next we apply a time-dependent displacement to both the bosonic field operators \hat{a} and the Holstein-Primakoff bosons \hat{b} ,

$$\hat{D}_{\hat{a}}(\alpha(t)) = \exp(\alpha(t)\hat{a}^\dagger - \alpha^*(t)\hat{a}), \quad (44)$$

$$\hat{D}_{\hat{b}}(\beta(t)) = \exp(\beta(t)\hat{b}^\dagger - \beta^*(t)\hat{b}). \quad (45)$$

This transformation takes into account the fact that the bosonic field operators and the atomic ensemble may acquire a macroscopic occupations. In the thermodynamic limit ($j \rightarrow \infty$) we find the following equations for the

displacement parameters $\alpha(t)$ and $\beta(t)$:

$$i\dot{\alpha} - \omega\alpha - \lambda\sqrt{\frac{2j - \beta\beta^*}{2j}} (\beta^* e^{i\phi(t)} + \beta e^{-i\phi(t)}) = 0, \quad (46)$$

$$-i\dot{\alpha}^* - \omega\alpha^* - \lambda\sqrt{\frac{2j - \beta\beta^*}{2j}} (\beta^* e^{i\phi} + \beta e^{-i\phi}) = 0, \quad (47)$$

$$i\dot{\beta} - \omega_0\beta - \lambda\sqrt{\frac{2j - \beta\beta^*}{2j}} (\alpha + \alpha^*) e^{i\phi} + \frac{1}{2}\lambda \frac{1}{\sqrt{2j}} \frac{1}{\sqrt{2j - \beta\beta^*}} (\alpha + \alpha^*) (\beta^* e^{i\phi} + \beta e^{-i\phi}) \beta = 0, \quad (48)$$

$$-i\dot{\beta}^* - \omega_0\beta^* - \lambda\sqrt{\frac{2j - \beta\beta^*}{2j}} (\alpha + \alpha^*) e^{-i\phi} + \frac{1}{2}\lambda \frac{1}{\sqrt{2j}} \frac{1}{\sqrt{2j - \beta\beta^*}} (\alpha + \alpha^*) (\beta^* e^{i\phi} + \beta e^{-i\phi}) \beta^* = 0, \quad (49)$$

which are equivalent to the system of equations obtained by the mean field approximation (26)-(29) if we use the following identification

$$\beta = \frac{1}{\sqrt{2}} (q_1 + ip_1), \quad \alpha = \frac{1}{\sqrt{2}} (q_2 + ip_2). \quad (50)$$

IV. RESULTS FOR THE MEAN PHOTON NUMBER AND THE PARITY

In this Section we study the time evolution of the scaled mean photon number and the parity for the rotated Dicke model. We explore several initial states and compare the results between driven and undriven situations. Namely, we consider several physically-relevant initial states: (i) coherent states $|\alpha\rangle|\zeta\rangle$, (ii) Fock state $|n=0\rangle|j, m=-j\rangle$ and (iii) the ground state $|\text{GS}\rangle$. Before going into detailed studies we introduce important observables and review the details of numerical procedure.

A. General setup

1. Mean photon number

The scaled mean photon number for the rotationally driven Dicke model is defined by

$$\begin{aligned} \frac{1}{j} \langle \hat{a}^\dagger \hat{a} \rangle &= \frac{1}{j} \langle \psi(t_f) | \hat{a}^\dagger \hat{a} | \psi(t_f) \rangle \\ &= \frac{1}{j} \langle \psi(t_0) | \hat{U}^\dagger(t_f) \hat{a}^\dagger \hat{a} \hat{U}(t_f) | \psi(t_0) \rangle, \end{aligned} \quad (51)$$

where the evolution operator is the time ordered exponent

$$\hat{U}(t) = \mathcal{T} \exp \left(-i \int_{t_0}^t dt' \hat{H}_{\text{RD}}(t') \right). \quad (52)$$

In particular we will focus on the dependence of $\frac{1}{j} \langle \hat{a}^\dagger \hat{a} \rangle$ on the coupling strength λ and the rotation velocity δ_ϕ after one or many revolutions for different initial states. Specifically, we are interested in the effect of the time-dependent rotation on the mean photon number. This gives us an insight into the interplay of the geometric phase and non-equilibrium time evolution.

In the TDL ($j \rightarrow \infty$) the time evolution of the scaled mean photon number can be derived from the time dependent mean field equations (26)-(29). Indeed

$$\frac{1}{j} \langle \hat{a}^\dagger \hat{a} \rangle = \frac{1}{j} |\alpha(t_f)|^2 = \frac{1}{2j} (q_2(t_f)^2 + p_2(t_f)^2) \quad (53)$$

if the system is initially (at $t = t_0$) prepared in the product state

$$|\psi(t_0)\rangle = |\alpha(t_0)\rangle |\zeta(t_0)\rangle \quad (54)$$

of the field coherent state $|\alpha\rangle$ and the spin coherent state $|\zeta\rangle$,

$$|\alpha(t)\rangle = e^{-\frac{1}{2}\alpha\alpha^*} \sum_{n=0}^{\infty} \frac{\alpha^n}{\sqrt{n!}} |n\rangle, \quad (55)$$

$$|\zeta(t)\rangle = \frac{1}{(1 + \zeta\zeta^*)^j} \sum_{m=-j}^j \zeta^{m+j} \sqrt{\binom{2j}{m+j}} |j, m\rangle. \quad (56)$$

2. Parity operator

An additional information on dynamical behavior is provided by the observable, which has a meaning of discrete topological number, namely the parity of a time-evolved state. The parity operator $\hat{\Pi}$ of the Dicke model reads

$$\hat{\Pi} = \exp \left(i\pi \hat{N} \right), \quad (57)$$

where

$$\hat{N} = \hat{a}^\dagger \hat{a} + \hat{J}_z + j \quad (58)$$

counts the number of excited quanta in the system. Applying it to a basis state $|n\rangle|j, m\rangle$ yields

$$\hat{\Pi}|n\rangle|j, m\rangle = e^{i\pi(n+m+j)} |n\rangle|j, m\rangle, \quad (59)$$

since $\hat{a}^\dagger \hat{a}|n\rangle = n|n\rangle$, $\hat{J}_z|j, m\rangle = m|j, m\rangle$ and $\hat{J}^2|j, m\rangle = j(j+1)|j, m\rangle$. Thus the parity operator has the eigenstates $|n\rangle|j, m\rangle$ and the corresponding eigenvalues ± 1 (depending whether $n + m + j$ is even or odd).

The time evolution of the parity operator is given by

$$\langle \psi(t) | \hat{\Pi} | \psi(t) \rangle = \sum_{n=0}^{\infty} \sum_{m=-j}^j |\kappa_{n,m}(t)|^2 e^{i\pi(n+m+j)}, \quad (60)$$

where $\kappa_{n,m}(t)$ is defined by the expansion of a state $|\psi(t)\rangle$ in the basis $|n\rangle|j, m\rangle$, i.e.,

$$|\psi(t)\rangle = \sum_{n=0}^{\infty} \sum_{m=-j}^j \kappa_{n,m}(t) |n\rangle|j, m\rangle. \quad (61)$$

In the TDL ($j \rightarrow \infty$) we use the solutions of the mean field equations (26)-(29)

$$\alpha = \frac{1}{\sqrt{2}} (q_2 + ip_2), \quad \zeta = \frac{q_1 + ip_1}{\sqrt{4j - (q_1^2 + p_1^2)}} \quad (62)$$

to calculate the time evolution of the parity for the dynamics starting from a coherent state $|\psi(t_0)\rangle = |\alpha(t_0)\rangle |\zeta(t_0)\rangle$. The time evolution of the parity can be calculated by using the following properties of the field coherent states

$$e^{i\pi \hat{a}^\dagger \hat{a}} |\alpha\rangle = |\beta\rangle, \quad \beta := e^{i\pi} \alpha, \quad (63)$$

$$\langle \alpha | \beta \rangle = \exp \left[\alpha^* \beta - \frac{1}{2} (\alpha^* \alpha + \beta^* \beta) \right], \quad (64)$$

$$\exp(\mu \hat{a}^\dagger \hat{a}) = \sum_{k=0}^{\infty} \frac{(e^\mu - 1)^k}{k!} (\hat{a}^\dagger)^k (\hat{a})^k \quad (65)$$

and the spin coherent states

$$e^{i\pi \hat{J}_z} |\zeta\rangle = |\eta\rangle e^{i\pi(-j)}, \quad \eta := e^{i\pi} \zeta, \quad (66)$$

$$\langle \zeta | \eta \rangle = \frac{(1 + \eta\zeta^*)^{2j}}{(1 + \zeta\zeta^*)^j (1 + \eta\eta^*)^j}. \quad (67)$$

The time evolution of the parity in the coherent state $|\alpha\rangle|\zeta\rangle$ therefore reads

$$\langle \alpha | \langle \zeta | \hat{\Pi} | \zeta \rangle | \alpha \rangle = \exp \left(\alpha \alpha^* (e^{i\pi} - 1) \right) \left(\frac{1 - \zeta \zeta^*}{1 + \zeta \zeta^*} \right)^{2j}. \quad (68)$$

3. Numerical procedure

For a finite number of two-level atoms $N = 2j$ or pseudo-spin of finite length $j = N/2$ the time evolution can not be calculated exactly. In addition, to study the validity of the time dependent mean field evolution equations we compare the mean field solution with exact numerical solution of the Schrödinger equation. For the numerical calculations we truncate the bosonic Hilbert space up to n_M bosons but we always keep the full Hilbert space of the pseudo-spin. We kept n_M always high enough to assure that the error of the numerical data is on the level of the machine precision. For the numerical solution we use the Chebyshev scheme [24] to

calculate the time evolution. First, we apply a transformation into a co-rotating basis $|\psi\rangle_{\text{ROT}} = \hat{R}_z(t)|\psi\rangle$:

$$\begin{aligned} \langle \hat{a}^\dagger \hat{a} \rangle &= \langle \psi(t_f) | \hat{a}^\dagger \hat{a} | \psi(t_f) \rangle \\ &= \text{ROT} \langle \psi(t_0) | e^{i\hat{H}_{\text{ROT}}t_f} \hat{a}^\dagger \hat{a} e^{-i\hat{H}_{\text{ROT}}t_f} | \psi(t_0) \rangle_{\text{ROT}}. \end{aligned} \quad (69)$$

Then we compute the time propagator of the time independent Hamiltonian

$$\hat{H}_{\text{ROT}} = (\omega_0 + \delta_\phi) \hat{J}_z + \omega \hat{a}^\dagger \hat{a} + \frac{\lambda}{\sqrt{2j}} (\hat{a}^\dagger + \hat{a}) (\hat{J}_+ + \hat{J}_-), \quad (70)$$

which is then expanded in a Chebyshev series:

$$e^{-i\hat{H}_{\text{ROT}}\Delta t} \approx \sum_{k=0}^M a_k T_k(\hat{h}_{\text{ROT}}), \quad (71)$$

where $T_k(\hat{h}_{\text{ROT}})$ are the Chebyshev polynomials of order k and \hat{h}_{ROT} is a rescaled Hamiltonian

$$\hat{h}_{\text{ROT}} = \frac{2\hat{H}_{\text{ROT}} - (E_{\text{Max}} + E_{\text{Min}})\hat{1}}{E_{\text{Max}} - E_{\text{Min}}}. \quad (72)$$

Here E_{Max} and E_{Min} are the largest and the smallest eigenvalue of \hat{H}_{ROT} . The expansion coefficients a_k are determined by

$$\begin{aligned} a_k &= (-i)^k \exp\left(-i\Delta t \frac{1}{2}(E_{\text{Max}} + E_{\text{Min}})\right) (2 - \delta_{k,0}) \\ &\quad J_k\left(\Delta t \frac{1}{2}(E_{\text{Max}} - E_{\text{Min}})\right), \end{aligned} \quad (73)$$

where $\delta_{k,0}$ is the Kronecker delta and $J_k(x)$ are the Bessel functions of the first kind.

In the same way we also compute the time evolution of the parity operator for a system with a finite number of two-level atoms.

B. Stationary Dicke initial state: $|\alpha_{\text{cst}}\rangle|\zeta_{\text{cst}}\rangle$

First, we study the mean photon number if the system is initially (at $t_0 = 0$) prepared in the product state of the field and spin coherent states

$$|\psi(0)\rangle = |\alpha_{\text{cst}}\rangle \otimes |\zeta_{\text{cst}}\rangle \quad (74)$$

with

$$\alpha_{\text{cst}} = \begin{cases} \frac{2\lambda}{\omega} \sqrt{j \left(1 - \left(\frac{\omega\omega_0}{4\lambda^2}\right)^2\right)}, & \lambda \geq \frac{1}{2}\sqrt{\omega\omega_0} \\ 0, & \lambda < \frac{1}{2}\sqrt{\omega\omega_0} \end{cases}, \quad (75)$$

$$\zeta_{\text{cst}} = \begin{cases} -\sqrt{\frac{4\lambda^2 - \omega\omega_0}{4\lambda^2 + \omega\omega_0}}, & \lambda \geq \frac{1}{2}\sqrt{\omega\omega_0} \\ 0, & \lambda < \frac{1}{2}\sqrt{\omega\omega_0} \end{cases}. \quad (76)$$

Coherent state with these parameters corresponds to the stationary state of the time independent (unrotated)

Dicke model (equations (26)-(29) for $\delta_\phi = 0$). This can be seen by inverting the parametrization used previously, see Eq. (20) and Eq. (21). Therefore, we obtain

$$q_1(0) = \begin{cases} -\sqrt{2j \left(1 - \frac{\omega\omega_0}{4\lambda^2}\right)}, & \lambda \geq \frac{1}{2}\sqrt{\omega\omega_0} \\ 0, & \lambda < \frac{1}{2}\sqrt{\omega\omega_0} \end{cases}, \quad (77)$$

$$p_1(0) = 0, \quad (78)$$

$$q_2(0) = \begin{cases} \frac{2\lambda}{\omega} \sqrt{j \left(1 - \left(\frac{\omega\omega_0}{4\lambda^2}\right)^2\right)}, & \lambda \geq \frac{1}{2}\sqrt{\omega\omega_0} \\ 0, & \lambda < \frac{1}{2}\sqrt{\omega\omega_0} \end{cases}, \quad (79)$$

$$p_2(0) = 0. \quad (80)$$

Our driving protocol is the following: we start in the initial state $|\alpha_{\text{cst}}\rangle|\zeta_{\text{cst}}\rangle$ and then we switch on the rotation at $t_0 = 0$ and let the system evolve until $t_f = n_R 2\pi/\delta_\phi$, where n_R indicates the number of rotations. In order to understand the influence of the rotation we also computed the time evolution where we do not switch on the rotation at $t_0 = 0$ but where we let the system evolve according to the usual Dicke Hamiltonian \hat{H}_D .

1. Time dependence of the mean photon number

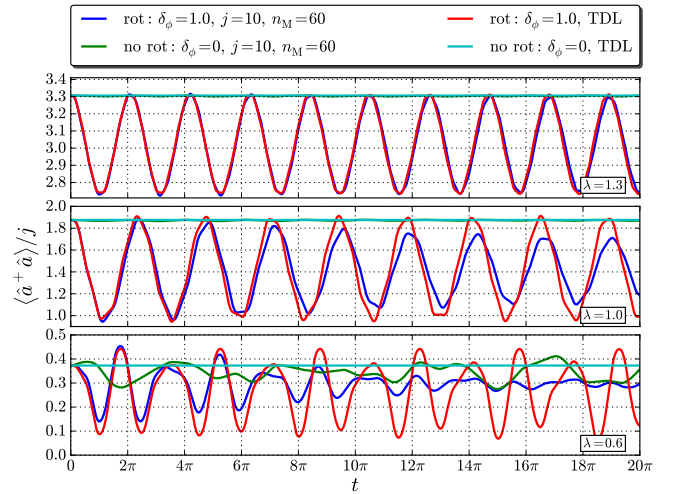


Figure 3: Time dependence of the scaled mean photon number on resonance $\omega = \omega_0 = 1.0$ for different values of the coupling strength $\lambda = 0.6, 1.0, 1.3$. The red and cyan curves are the time evolution obtained from the time dependent mean field equations and the blue and green from the numerical integration of the time dependent Schrödinger equation for a finite sized system. Here the red and blue lines correspond to rotationally driven system with a driving velocity of $\delta_\phi = 1.0$ and the cyan and green curves correspond to the time evolution with no rotational driving.

Fig. 3 compares the time evolution of the scaled mean photon number, $\langle \hat{a}^\dagger \hat{a} \rangle(t)/j$ for the rotationally driven Dicke model and the time evolution of the undriven Dicke

model. Part of the data refer to the TDL at $j \rightarrow \infty$, using the mean field solution (red and cyan), while the other part corresponds to the system with a finite number of two level atoms (blue and green). We observe that the mean field solution works very well in the strong coupling regime and it becomes more and more accurate with increasing j , as expected.

2. Dependence of the mean photon number on the atom-field coupling strength λ

The dependence of the scaled mean photon number on the coupling strength λ after time evolution of the system corresponding to a single circle, $t_f = 2\pi/\delta_\phi$, is shown in Fig. 4 for a fixed driving velocity $\delta_\phi = 1.0$ and on resonance $\omega = \omega_0 = 1.0$. Again, the mean photon

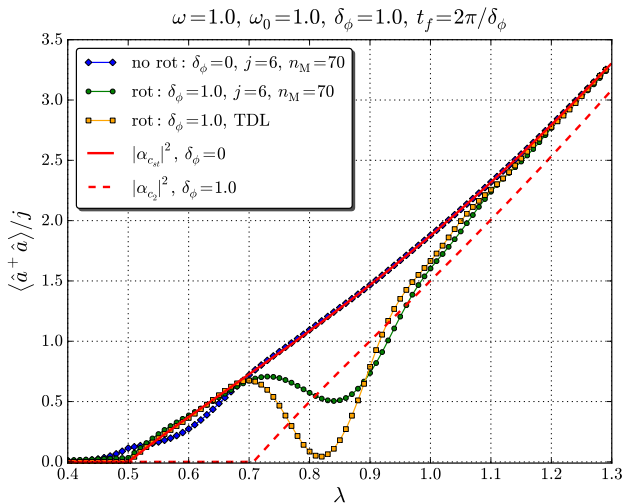


Figure 4: The scaled mean photon number as a function of the coupling strength. Comparing the mean field solution ($j \rightarrow \infty$) with the numerical solution for a system with a finite number of atoms. We also compare the rotationally driven Dicke model with the undriven Dicke model.

number is computed using the time dependent mean field equations which should be valid in the TDL ($j \rightarrow \infty$, see orange curve) and also by solving the Schrödinger equation numerically (here $j = 6$, see green curve). We also compare the results with the evolution of the Dicke model in the absence of rotations (blue curve).

A clear feature of the rotational driving is the appearance of a minimum in the super radiant phase (in the case of the Fig. 4 around $\lambda \approx 0.82$). By looking into the time evolution of the scaled mean photon number we observe from Fig. 3 that the time evolution is not periodic in the region of the minimum which may be attributed to the onset of chaotic behavior noticed in Ref. [18]. The new minimum is an indication of the competition between two stationary states, corresponding to driven and unrotated

Dicke models.

Now let us consider an interesting limit of multiple rotations $\phi_f \gg 1$. This limit is interesting because of a competition between dynamical and geometric phases [14]. In this limit it is natural to look into the time averaged scaled mean photon number

$$\langle \langle \hat{a}^\dagger \hat{a} \rangle \rangle_T / j := \frac{1}{t_f - t_0} \int_{t_0}^{t_f} dt \langle \hat{a}^\dagger \hat{a} \rangle / j. \quad (81)$$

In Fig. 5 we illustrate the time averaged scaled mean photon number obtained for a fixed rotation velocity $\delta_\phi = 1.0$ by solving the mean field equations (orange curve) and by solving the Schrödinger equation for a system with $j = 6$ (green curve). We conclude therefore that

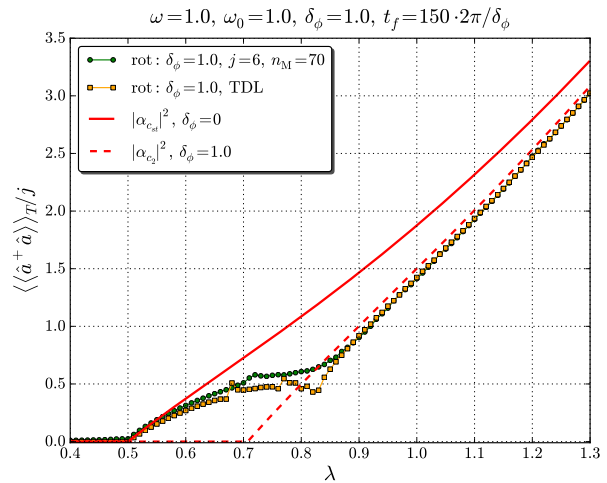


Figure 5: Time averaged mean photon number as a function of λ . The presence of a new minimum in the super radiant phase indicates a reentrant behavior as a consequence of a competition between geometric and dynamical phases [14].

the averaging over many rotation reveals a meta-stable phase in the super-radiant phase $\lambda > \lambda_c$. This phase is determined by a dynamical critical atom-field coupling strength $\lambda_c^{(\text{dyn})}$. In the case of $\omega = \omega_0 = 1.0$ and $\delta_\phi = 1.0$ it is given by $\lambda_c^{(\text{dyn})} \approx 0.82$.

3. Dependence of the mean photon number on the rotation velocity δ_ϕ

The dependence of the scaled mean photon number on the driving velocity after evolving the system for one circle $t_f = 2\pi/\delta_\phi$, with different atom-field coupling parameters λ is plotted in Fig. 6. We observe that if the critical paraboloid is not encircled $\lambda < \lambda_c = \sqrt{\omega\omega_0}/2$, the mean photon number is zero. But if we encircle the critical paraboloid the mean photon number is non-zero and there should be a critical driving velocity. Similar to the case of the stationary state of the rotated Dicke

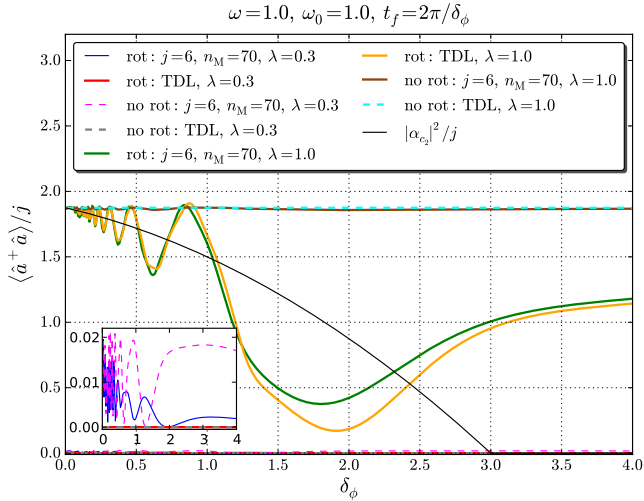


Figure 6: The driving velocity dependence of the scaled mean photon number after a single circle.

model, where the critical atom-field coupling is given by $\sqrt{\omega(\omega_0 + \delta_\phi)}/2$ which defines a critical driving velocity $\delta_{\phi,c}^{(\text{rot})}$ (see the black curve in Fig. 6: $|\alpha_{c_2}|^2/j$). Note however that in the case of one rotation we can not see an indication of presence of the critical driving velocity in the dynamics.

In Fig. 7 we also plot the time averaged scaled mean photon number which clearly illustrate the presence of a dynamical or rotational critical driving velocity $\delta_{\phi,c}^{(\text{dyn})}$ in the TDL.

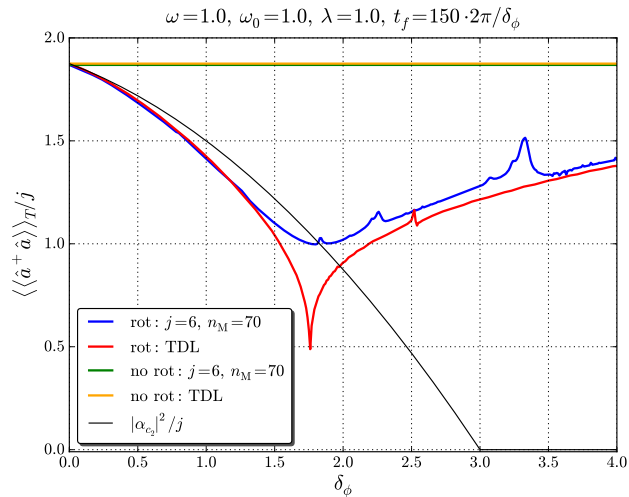


Figure 7: Time averaged scaled mean photon number as a function of the rotation velocity. We compare $\langle \langle \hat{a}^\dagger \hat{a} \rangle \rangle_T / j$ for the rotationally driven Dicke model with the one for the undriven Dicke model. In both cases we kept $t_f = 150 \cdot 2\pi/\delta_\phi$.

4. Non-Equilibrium Phase Diagram

Summarizing our studies, in Fig. 8 we plot the time averaged scaled mean photon number as a function of the driving velocity and the atom-field coupling strength obtained from the mean field equations (26)-(29). One can clearly distinguish two distinct “meta stable” phases in the super-radiant phase. We therefore suggest this plot as a non-equilibrium phase diagram of the rotationally driven Dicke model. We associate this reentrant behavior with a competition between geometric and dynamical phases. This mechanism is described in Ref. [14].

The line in the super-radiant phase (the red dashed curve in Fig. 8) which describes a dynamical critical line, was fitted with the function $\lambda_c^{(\text{dyn})} = 0.5 + 0.327\delta_\phi^{3/4}$. It defines a dynamical critical atom-field coupling strength $\lambda_c^{(\text{dyn})}$ or reciprocally a dynamical critical driving velocity $\delta_{\phi,c}^{(\text{dyn})}$. This should not be confused with the critical coupling $\lambda_c^{(\text{rot})} = \sqrt{\omega(\omega_0 + \delta_\phi)}/2$, that emerges if we start the evolution of a system from the stationary state $|\alpha_{c_2}\rangle|\zeta_{c_2}\rangle$ (see next paragraph).

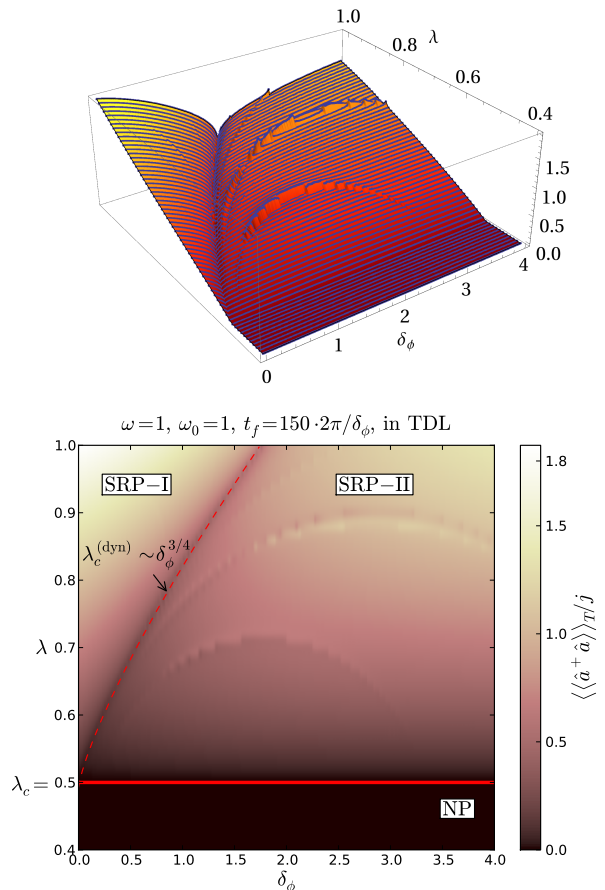


Figure 8: Dependence of the time averaged scaled mean photon number on velocity of rotation and the atom-field coupling strength. It is obtained from the mean field equations for $\omega = \omega_0 = 1.0$ and averaged over a time $t_f = 150 \cdot 2\pi/\delta_\phi$.

5. Parity $\hat{\Pi}$

In Fig. 9 we show the time evolution of the parity operator starting in the coherent state $|\alpha_{\text{st}}\rangle|\zeta_{\text{st}}\rangle$ for a system with a finite number of two-level atoms. The parity is constant in time and once we enter a super-radiant phase $\lambda > \lambda_c = \sqrt{\omega\omega_0}/2$ it starts to drop from one to zero. The inset plot shows the λ dependence of the parity and its tendency to a step function with growing j .

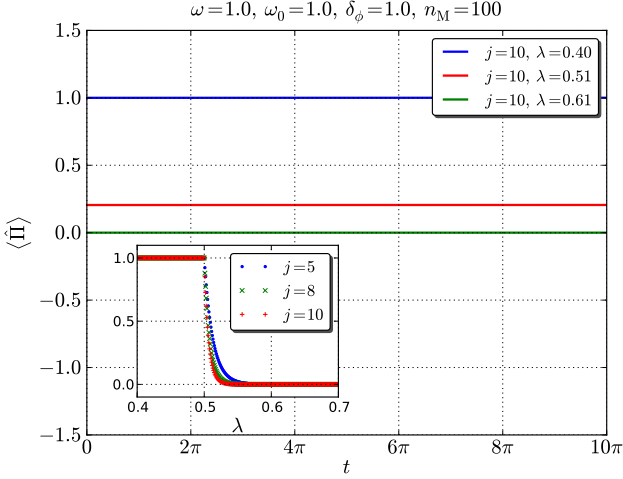


Figure 9: Time evolution of the parity operator when we start the dynamics in the coherent state $|\alpha_{\text{st}}\rangle|\zeta_{\text{st}}\rangle$ for a system with a finite number of atoms. The inset plot shows the dependence on the coupling constant λ for different values of j .

The time evolution of the parity $\langle \hat{\Pi} \rangle$ and its dependence on the atom-field coupling λ calculated from the mean field equations, i.e., by Eq. (68), is shown in Fig. 10. The parity is not a constant function of time in the previously observed intermediate regime of $\langle \hat{a}^\dagger \hat{a} \rangle / j$. The time averaged parity as well reveals the observed dynamical critical coupling $\lambda_c^{(\text{dyn})} \approx 0.82$. Nevertheless, for $j \rightarrow \infty$ the parity becomes constant in time and goes to 0 in the entire super-radiant phase.

Further, in Fig. 11 we also illustrate the scaled parity, namely the parity where all the phase space coordinates (q_i, p_i) are rescaled by \sqrt{j} : $(q_i, p_i) \rightarrow (q_i/\sqrt{j}, p_i/\sqrt{j})$. This implies

$$\langle \alpha | \langle \zeta | \hat{\Pi}_{\text{sc}} | \zeta \rangle | \alpha \rangle = \exp\left(\frac{1}{2j}(q_2^2 + p_2^2)(e^{i\pi} - 1)\right) \left(1 - \frac{q_1^2 + p_1^2}{2j^2}\right)^{2j}. \quad (82)$$

The scaled parity is naturally independent of the number of spins j but it is no longer constant in time for couplings between 0.5 and 1. The time averaged scaled parity shows also an intermediate regime similar to the intermediate regime in the time averaged scaled mean photon number.

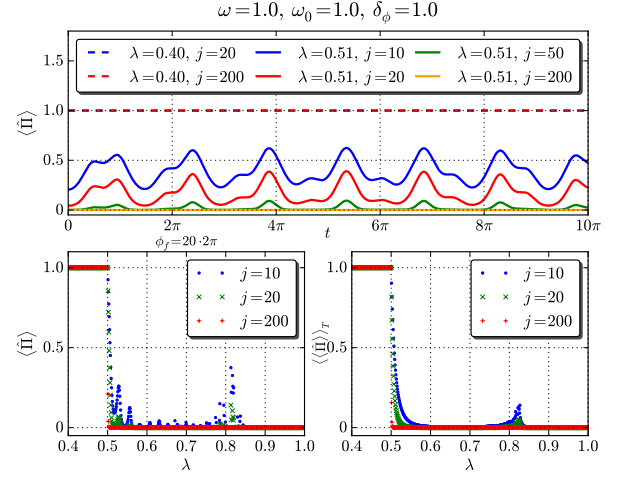


Figure 10: Upper panel: time evolution of the parity operator if we start the dynamics in the coherent state $|\alpha_{\text{st}}\rangle|\zeta_{\text{st}}\rangle$. Lower left panel: the dependence on the atom-field coupling constant λ of the parity after 20 circle. Lower right panel: the dependence of the time averaged parity on the coupling constant λ . The parity is obtained by solving the time dependent mean field equations.

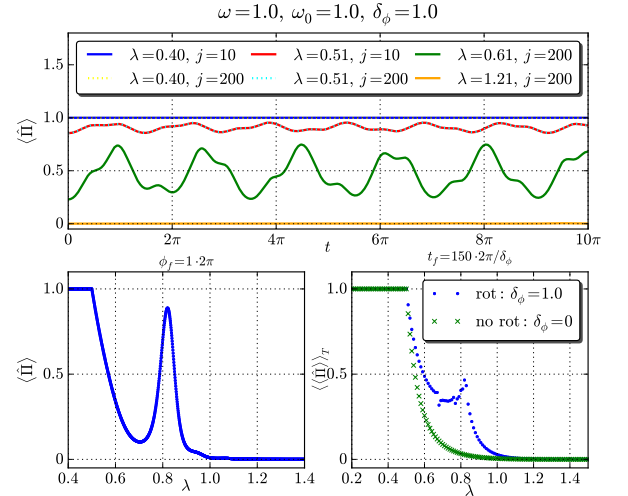


Figure 11: Upper panel: time evolution of the scaled parity operator if we start the dynamics in the coherent state $|\alpha_{\text{st}}\rangle|\zeta_{\text{st}}\rangle$. Lower left panel: the dependence of the scaled parity on the coupling constant λ after one circle. Lower right panel: the dependence of the time averaged scaled parity on the coupling constant λ . The scaled parity was computed by solving the time dependent mean field equations.

C. Stationary circle initial state: $|\alpha_{c_2}\rangle|\zeta_{c_2}\rangle$

Here we study the mean photon number if the system is initially (at $t_0 = 0$) prepared in the product state of

the field and spin coherent states

$$|\psi(0)\rangle = |\alpha_{c_2}\rangle \otimes |\zeta_{c_2}\rangle, \quad (83)$$

with

$$\alpha_{c_2} = \begin{cases} \frac{2\lambda}{\omega} \sqrt{\frac{j}{2} \left(1 - \left(\frac{\Omega}{4\lambda^2}\right)^2\right)} & \text{if } \lambda \geq \frac{1}{2}\sqrt{\Omega} \\ 0 & \text{if } \lambda < \frac{1}{2}\sqrt{\Omega} \end{cases}, \quad (84)$$

$$\zeta_{c_2} = \begin{cases} -\sqrt{\frac{4\lambda - \Omega}{4\lambda + \Omega}} & \text{if } \lambda \geq \frac{1}{2}\sqrt{\Omega} \\ 0 & \text{if } \lambda < \frac{1}{2}\sqrt{\Omega} \end{cases}. \quad (85)$$

where $\Omega = \omega(\omega_0 + \delta_\phi)$. This choice of the parameters α and ζ of the coherent states corresponds to the stationary ‘‘circle’’ solutions of the time dependent mean field equations (26)-(29). In the same way as in the previous section this can be obtained using Eq. (20) which gives

$$q_1(0) = \begin{cases} -\sqrt{2j \left(1 - \frac{\Omega}{4\lambda^2}\right)}, & \lambda \geq \frac{1}{2}\sqrt{\Omega} \\ 0, & \lambda < \frac{1}{2}\sqrt{\Omega} \end{cases}, \quad (86)$$

$$p_1(0) = 0, \quad (87)$$

$$q_2(0) = \begin{cases} \frac{2\lambda}{\omega} \sqrt{j \left(1 - \left(\frac{\Omega}{4\lambda^2}\right)^2\right)}, & \lambda \geq \frac{1}{2}\sqrt{\Omega} \\ 0, & \lambda < \frac{1}{2}\sqrt{\Omega} \end{cases}, \quad (88)$$

$$p_2(0) = 0. \quad (89)$$

The driving protocol is the following: we start with the system prepared in the state $|\alpha_{c_2}\rangle|\zeta_{c_2}\rangle$. Then we switch on the rotation at $t_0 = 0$ and let the system evolve according to $\hat{H}_{\text{RD}}(t)$ until $t_f = n_{\text{R}} 2\pi/\delta_\phi$. Here n_{R} indicates the number of rotations in the space of parameters (see Fig. 1). Further, we consider the time evolution where we do not switch on the rotation at $t_0 = 0$ but where we evolve the system according to \hat{H}_{D} (undriven case) in order to understand the influence of the rotational driving.

1. Mean photon number for the stationary coherent state

From the fixed point solution of the equations of motions (26)-(29) we observe that if we start the evolution from the state (83), the dynamics of the system remains bounded to the circle and after a closed evolution $t_f = 2\pi/\delta_\phi$ the mean photon number in the thermodynamic limit is simply given by

$$\begin{aligned} \frac{1}{j} \langle \hat{a}^\dagger \hat{a} \rangle_{c_2} &= \frac{1}{j} \langle \zeta_{c_2} | \langle \alpha_{c_2} | \hat{a}^\dagger \hat{a} | \alpha_{c_2} \rangle | \zeta_{c_2} \rangle = \frac{1}{j} |\alpha_{c_2}|^2 = \frac{1}{2j} q_2^2 \\ &= \begin{cases} \frac{1}{2} \left(\frac{2\lambda}{\omega}\right)^2 \left[1 - \left(\frac{\Omega}{4\lambda^2}\right)^2\right] & \text{if } \lambda \geq \frac{1}{2}\sqrt{\Omega} \\ 0 & \text{if } \lambda < \frac{1}{2}\sqrt{\Omega} \end{cases} \end{aligned} \quad (90)$$

We also observe now that the critical coupling, which marks the quantum phase transition, is shifted by the amount of the rotation velocity as $\lambda_c^{(\text{rot})} = \frac{1}{2}\sqrt{\omega(\omega_0 + \delta_\phi)}$. In Fig. 12 (left) we plot $\langle \hat{a}^\dagger \hat{a} \rangle_{c_2}/j$ in order to illustrate the shift of the critical coupling caused

by the rotation. Further, in Fig. 12 (right) we draw the velocity dependence of $\langle \hat{a}^\dagger \hat{a} \rangle_{c_2}/j$ for circles \mathcal{C}_2 inside the critical paraboloid and compare it with the situation corresponding to circles \mathcal{C}_1 that encircle the critical paraboloid. One can see that the critical driving velocity is defined by $\delta_{\phi,c}^{(\text{rot})} = \frac{4\lambda^2}{\omega} - \omega_0$. Above this critical velocity the mean photon number is zero. This allows one to probe the equilibrium quantum critical point $\lambda_c = \sqrt{\omega\omega_0}/2$ in an indirect way by encircling critical paraboloid in the parameter space and measuring the dependence of mean photon number as a function of a driving velocity.

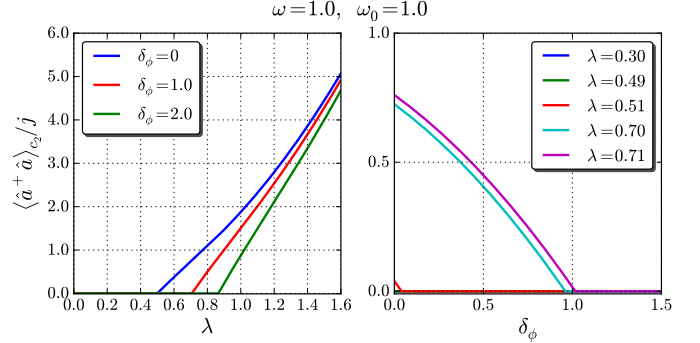


Figure 12: Plot of the mean photon number $\langle \hat{a}^\dagger \hat{a} \rangle_{c_2}/j$ as a function of the coupling strength λ on the left panel and as a function of the rotation velocity δ_ϕ on the right panel.

2. Deviation from stationary coherent state

The natural question which immediately arises is what happens if the initial state is not exactly given by the fixed point conditions, namely if the initial state is not a coherent state

$$|\alpha(t)\rangle = e^{-\frac{1}{2}\alpha\alpha^*} \sum_{n=0}^{\infty} \frac{\alpha^n}{\sqrt{n!}} |n\rangle \quad (91)$$

$$|\zeta(t)\rangle = \frac{1}{(1 + \zeta\zeta^*)^j} \sum_{m=-j}^j \zeta^{m+j} \sqrt{\binom{2j}{m+j}} |j, m\rangle \quad (92)$$

with $\alpha(0) = \alpha_{c_2}$ and $\zeta(0) = \zeta_{c_2}$. In Fig. (13) we plot the scaled mean photon number obtained from solving the time dependent mean field equations but this time with the initial condition that slightly differ from the fixed point.

3. Time dependence of the mean photon number

In Fig. 14 we illustrate the time evolution of the scaled mean photon number. In the TDL ($j \rightarrow \infty$) we used the time dependent mean field equations (26)-(29) in order to

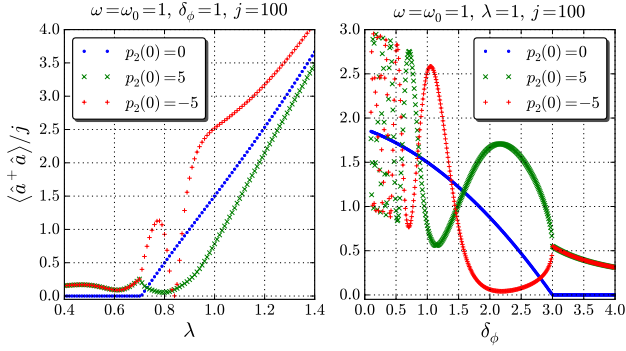


Figure 13: The mean photon number $\langle \hat{a}^\dagger \hat{a} \rangle_{c_2} / j$ as a function of the coupling strength λ on the left and as a function of the rotation velocity δ_ϕ on the right starting on the fixed point $(q_{1,c_2}, p_{1,c_2}, q_{2,c_2}, p_{2,c_2})$ (blue dots) and with small deviation from this fixed point (red + and green \times).

compute $\langle \hat{a}^\dagger \hat{a} \rangle(t) / j$ (orange curve) while for a finite number of two-level systems we used the Chebyshev technique to calculate the time evolution. We compare the time evolution of the scaled mean photon number of the rotationally driven Dicke model (solid lines in Fig. 14) with the time evolution of the scaled mean photon number of the Dicke model with no rotation of the pseudo-spin vector around the z axis (dashed lines in Fig. 14).

As expected, if we start in the coherent state $|\alpha_{c_2}\rangle|\zeta_{c_2}\rangle$ the time evolution of $\langle \hat{a}^\dagger \hat{a} \rangle / j$ is constant in the TDL (solid orange line in Fig. 14). However, for finite j one can see that the scaled mean photon number is not time independent, but increasing j it tends to a constant value (the amplitude of the oscillation decreases). In the case where we let the system evolve without rotational driving, the scaled mean photon number shows pronounced oscillatory behavior compared to the rotational driving which is not completely 2π periodic.

4. Dependence of the mean photon number on the atom-field coupling strength λ

In this subsection we illustrate the dependence of the scaled mean photon numbers on the atom-field coupling strength, $\langle \hat{a}^\dagger \hat{a} \rangle(\lambda) / j$. The system is initially prepared in the product coherent state $|\alpha_{c_2}\rangle|\zeta_{c_2}\rangle$. First we consider only one revolution in parameter space, $t_f = 2\pi/\delta_\phi$. For rotational driving the system remains in the same state and there is no significant deviation from the static behavior of the scaled mean photon number. However, if the system is evolved according to the usual Dicke model \hat{H}_D a peak is observed at $\lambda_c^{(\text{rot})}$. For $\lambda < \lambda_c^{(\text{rot})}$ there is a large discrepancy between the finite size calculation and the mean field solution.

In Fig. 16 we show the time averaged scaled mean photon number, $\langle \langle \hat{a}^\dagger \hat{a} \rangle_T \rangle / j$ as defined in Eq. 81 for the fixed rotation velocity $\delta_\phi = 1.0$. For a finite number of two-

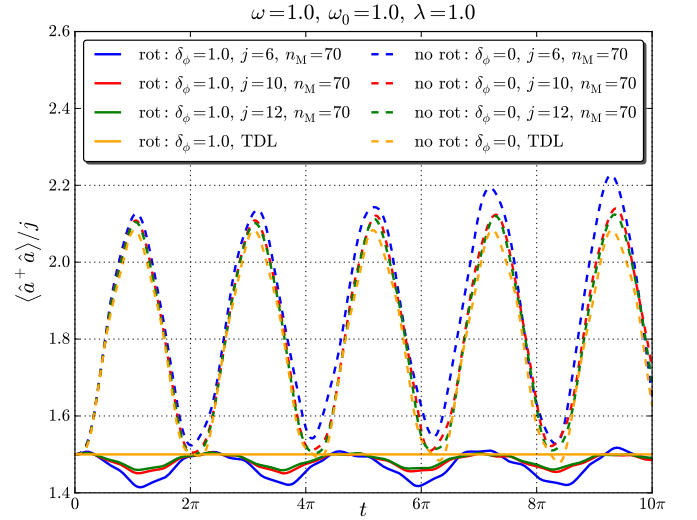


Figure 14: Time dependence of the scaled mean photon number, $\langle \hat{a}^\dagger \hat{a} \rangle / j$, for different values of j , a coupling $\lambda = 1.0$ and for $\omega = \omega_0 = 1.0$. The solid lines represent the time evolution with rotational driving and the dashed lines give the time evolution of the Dicke model without rotational driving. The evolution time t_f in both cases is the same.

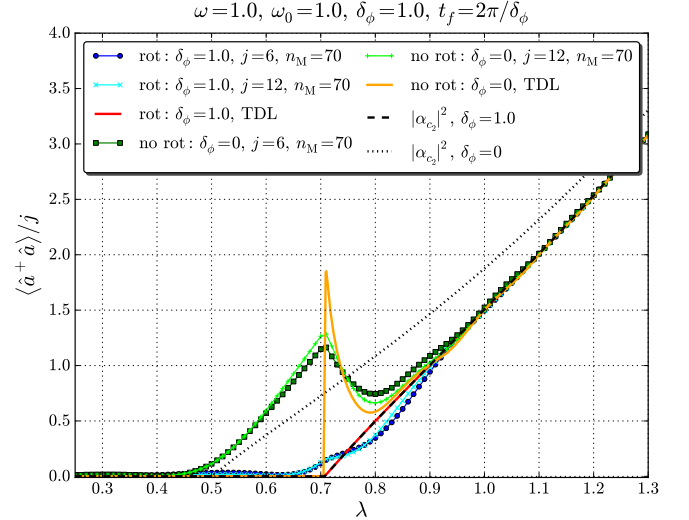


Figure 15: The scaled mean photon number as a function of the coupling strength λ . We compare $\langle \hat{a}^\dagger \hat{a} \rangle / j$ for the rotationally driven Dicke model with the one for undriven Dicke model ($t_f = 2\pi/\delta_\phi$ was kept the same in both cases).

level systems $N = 2j$ the time propagation was calculated using the Chebyshev scheme [24] and in the TDL we solved the time-dependent mean field equations.

For the initial state $|\alpha_{c_2}\rangle|\zeta_{c_2}\rangle$ which corresponds to the stationary state of \hat{H}_{RD} we effectively observe no difference between $|\alpha_{c_2}|^2 / j$ and the time evolved computations. However, when the system is evolved accord-

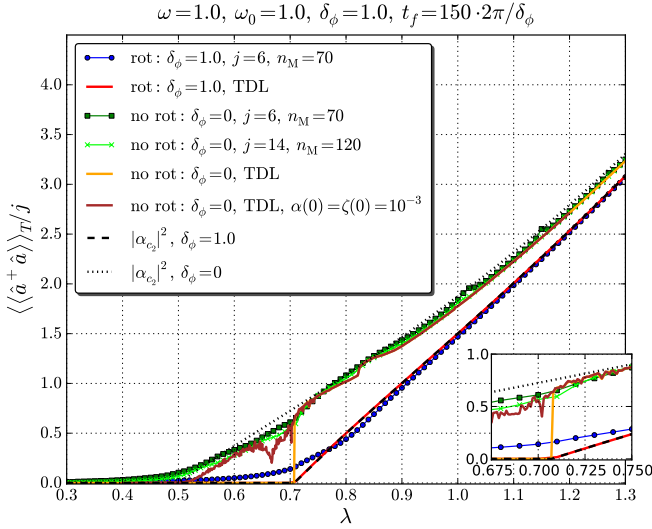


Figure 16: The time averaged scaled mean photon number as a function of the coupling strength λ . We compare $\langle\langle \hat{a}^\dagger \hat{a} \rangle\rangle_T / j$ for the rotationally driven Dicke model and the unrotated Dicke model (t_f was kept the same in both cases).

ing to \hat{H}_D we again observe that below $\lambda_c^{(\text{rot})}$ the finite size results do not coincide in both cases. This can be corrected if we introduce small fluctuations to the semi-classical description by setting the initial conditions of the mean field equations (26)-(29) not strictly to zero but $\alpha(0) = \zeta(0) = \alpha^*(0) = \zeta^*(0) = 10^{-3}$ (brown line).

5. Dependence of the mean photon number on the rotation velocity δ_ϕ

In this subsection we illustrate the dependence of the scaled mean photon number on the rotation velocity δ_ϕ after one revolution in parameter space, $t_f = 2\pi/\delta_\phi$, which is shown in Fig. 17. We observe that if the critical paraboloid is encircled, the scaled mean photon number is different from zero and the critical driving velocity is given by $\delta_{\phi,c}^{(\text{rot})} = \frac{4\lambda^2}{\omega} - \omega_0$. This basically follows from the rotation velocity shift in the rotated critical coupling $\lambda_c^{(\text{rot})} = \sqrt{\omega(\omega_0 + \delta_\phi)}/2$. This allows one to probe the equilibrium quantum critical point $\lambda_c = \sqrt{\omega\omega_0}/2$ from a distance in parameter space.

The velocity dependence of the time averaged scaled mean photon number (Fig. 18) clearly reveals the critical driving velocity $\delta_{\phi,c}^{(\text{rot})}$. However, if we suddenly, at $t_0 = 0$, switch on the undriven evolution (with \hat{H}_D) the mean field solution is zero for $\delta_\phi > \delta_{\phi,c}^{(\text{rot})}$ while the numerical calculation for a finite number of atoms is non zero in this region. Again, this can be corrected if we allow small fluctuations in the semi-classical description by setting the initial conditions of the mean field equations not strictly to zero: $\alpha(0) = \zeta(0) = \alpha^*(0) = \zeta^*(0) = 10^{-3}$

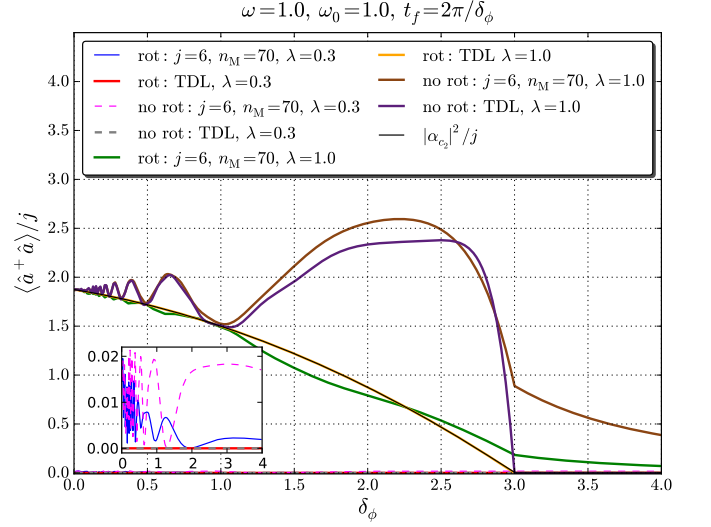


Figure 17: The scaled mean photon number as a function of the rotation velocity δ_ϕ . We compare $\langle\langle \hat{a}^\dagger \hat{a} \rangle\rangle_T / j$ for the rotationally driven Dicke model and for the unrotated Dicke model with $t_f = 2\pi/\delta_\phi$ in both cases.

in the corresponding range of the parameters.

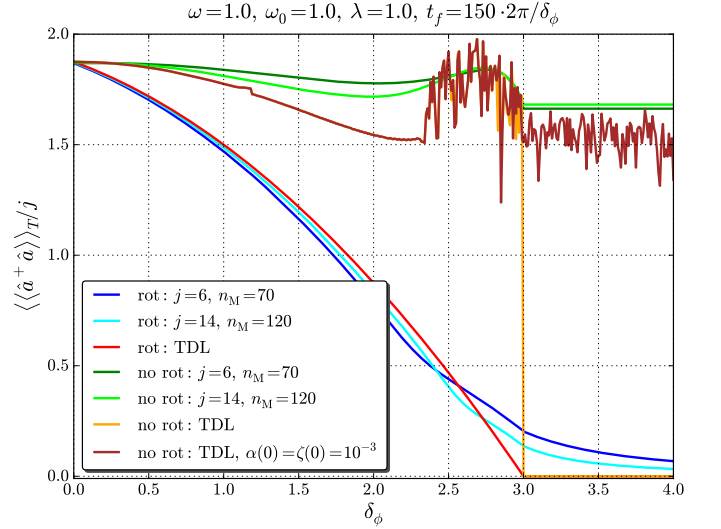


Figure 18: The time averaged scaled mean photon number as a function of the rotation velocity δ_ϕ . We compare $\langle\langle \hat{a}^\dagger \hat{a} \rangle\rangle_T / j$ for the rotationally driven Dicke model with the results for the unrotated Dicke model averaged over $t_f = 150 \cdot 2\pi/\delta_\phi$ in both cases.

6. Non-Equilibrium Phase Diagram

We summarize the dependence of the time averaged scaled mean photon number on the atom field-coupling

strength λ and the rotation velocity δ_ϕ in Fig. 19. Here we see that the rotational driving shifts the super-radiant phase transition by the amount given by the rotation velocity. The critical line (solid red line in Fig. 19) is defined by $\lambda_c^{(\text{rot})} = \sqrt{\omega(\omega_0 + \delta_\phi)}$ or by $\delta_{\phi,c}^{(\text{rot})} = \frac{4\lambda^2}{\omega} - \omega_0$.

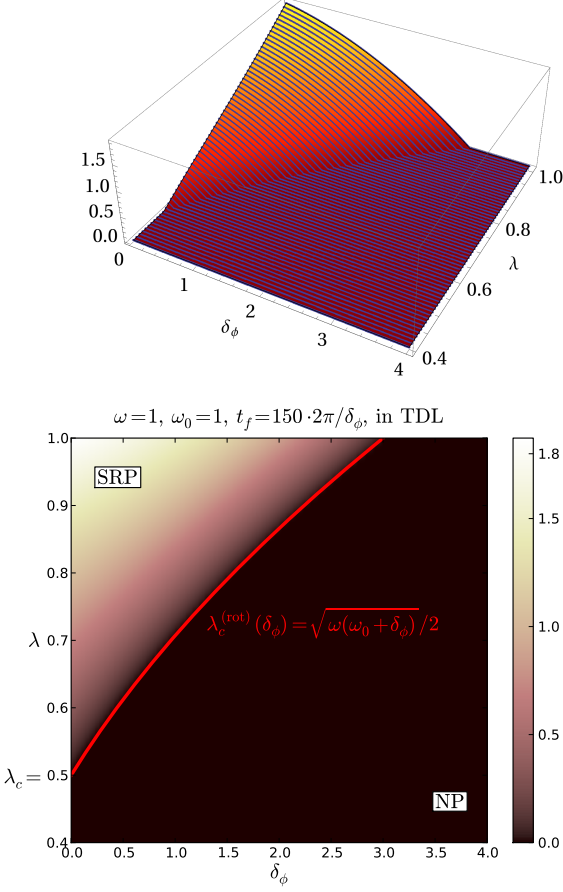


Figure 19: The time averaged scaled mean photon number as a function of the rotation velocity and the atom-field coupling strength. Results are obtained from the mean field equations for $\omega = \omega_0 = 1.0$ and averaged over a time $t_f = 150 \cdot 2\pi/\delta_\phi$.

7. Parity $\hat{\Pi}$

The time evolution of the parity operator $\langle \psi(t) | \hat{\Pi} | \psi(t) \rangle$ is calculated for the stationary circle initial state $|\alpha_{c_2}\rangle |\zeta_{c_2}\rangle$. Results are shown in Fig. 20 for a system with a finite number of two-level atoms. Note that the parity is constant in time and jumps from one to zero at the critical atom-field coupling strength $\lambda_c^{(\text{rot})}$.

In the TDL ($j \rightarrow \infty$) we use the solutions of the mean field equations to calculate the time evolution of the parity, Fig. 21. We also illustrate the time evolution of the scaled parity (where as previously we rescaled all the phase space coordinates by \sqrt{j}).

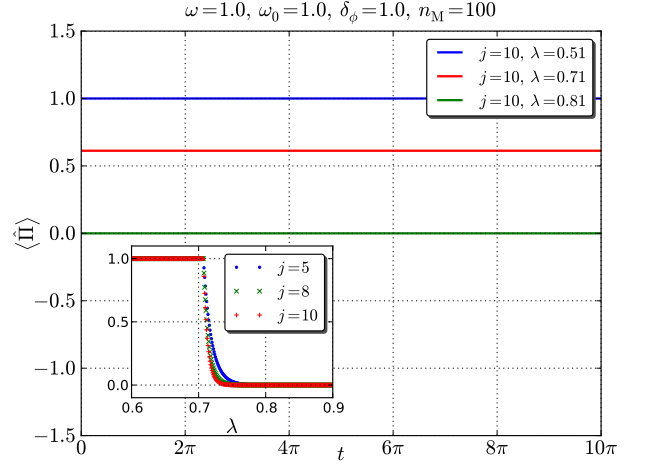


Figure 20: Time evolution of the parity operator starting from the coherent state $|\alpha_{c_2}\rangle |\zeta_{c_2}\rangle$ for a system of finite number of two-level atoms. The inset plot shows the dependence on the coupling constant λ for different values of j .

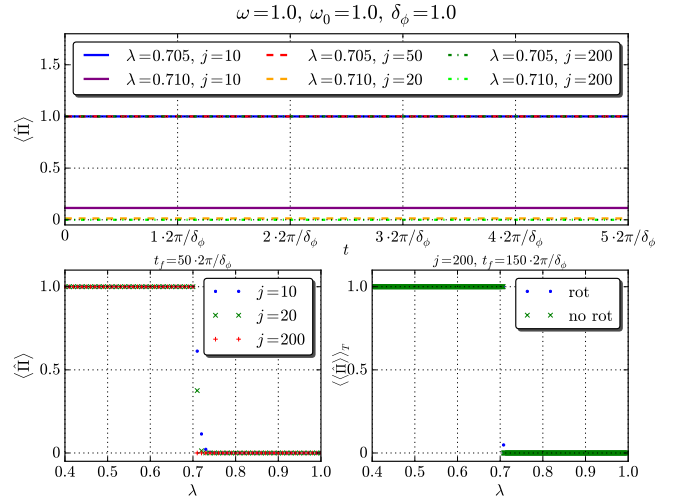


Figure 21: Upper panel: time evolution of the parity $\langle \hat{\Pi} \rangle$ starting from the coherent state $|\alpha_{c_2}\rangle |\zeta_{c_2}\rangle$. Lower left panel: dependence of $\langle \hat{\Pi} \rangle$ on the coupling constant λ for different values of j after 50 circles. Lower right panel: time averaged parity as a function of the coupling λ . The time evolution is calculated from the time dependent mean field equations.

D. Fock initial state: $|n=0\rangle |j, m=-j\rangle$

Here we consider the evolution of the mean photon number if we initially prepare the systems in the Fock state with no photons $n=0$ while the spin state has the lowest weight, $m=-j$,

$$|\psi(t_0=0)\rangle = |0\rangle \otimes |j, -j\rangle. \quad (93)$$

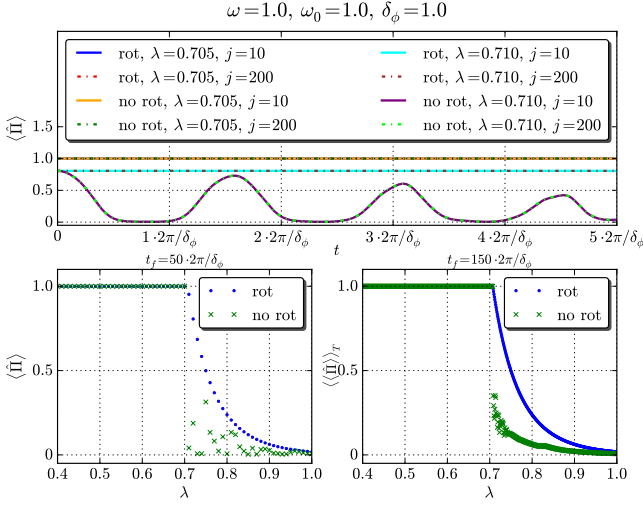


Figure 22: Upper panel: time evolution of the scaled parity operator starting from the coherent state $|\alpha_{c2}\rangle|\zeta_{c2}\rangle$. Lower left panel: the dependence on the coupling constant λ of the scaled parity. Lower right panel: the time averaged scaled parity as a function of λ .

We switch on the rotation at $t_0 = 0$ and let the system evolve until $t_f = n_R 2\pi/\delta_\phi$, where we measure the mean photon number $\langle \hat{a}^\dagger \hat{a} \rangle(t_f)/j$. We also compare it with the evolution of the un-rotated system. In terms of the coherent states this initial state corresponds to $\alpha = 0$ and $\zeta = 0$. The mean photon number is calculated in the TDL using the mean field equations (26)-(29) with the initial conditions $\alpha(0) = \alpha^*(0) = \zeta(0) = \zeta^*(0) = 0$.

1. Time evolution of the mean photon number

In Fig. 23 we show the time evolution of the scaled mean photon number, $\langle \hat{a}^\dagger \hat{a} \rangle/j$. It compares the scaled mean photon calculated for a system of finite size ($j = 6$) by the Chebyshev scheme with and without rotations (red and blue curve respectively) with results for the TDL ($j \rightarrow \infty$) with and without rotations (orange and green curve respectively).

In the static case the mean photon number is explicitly zero for this initial state, however for the driven situation we observe a critical coupling above which the scaled mean photon number becomes macroscopic. We observe that for the initial Fock state, $|0\rangle|j, -j\rangle$, the scaled mean photon number in the rotated case (we switch on the rotation at $t_0 = 0$) is still microscopic for $\lambda = 0.5$ whereas if no rotation is switched on the scaled mean photon number becomes macroscopic at $\lambda_c = \sqrt{\omega\omega_0}/2 = 0.5$. Therefore, the critical coupling λ_c is shifted by the amount given by the applied rotation velocity δ_ϕ . Thus for the driven case $\lambda_c^{(\text{rot})} = \sqrt{\omega(\omega_0 + \delta_\phi)}/2$.

Note that in the TDL the mean field equations do not reproduce the finite size calculations of the scaled mean

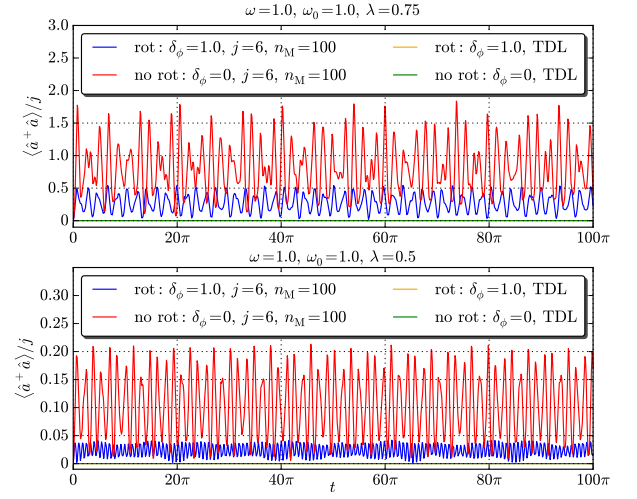


Figure 23: Time dependence of the scaled mean photon number on a resonance $\omega = \omega_0 = 1.0$ for different values of the coupling strength λ . The system is initially prepared in the state $|0\rangle|j, -j\rangle$.

photon number.

2. Dependence of the mean photon number on the atom-field coupling strength λ

Accordingly, we study the dependence of the scaled mean photon number on the atom-field coupling strength λ . First only for one closed circle in parameter space $\phi_f = 2\pi$, i.e., $t_f = 2\pi/\delta_\phi$. The scaled mean photon num-

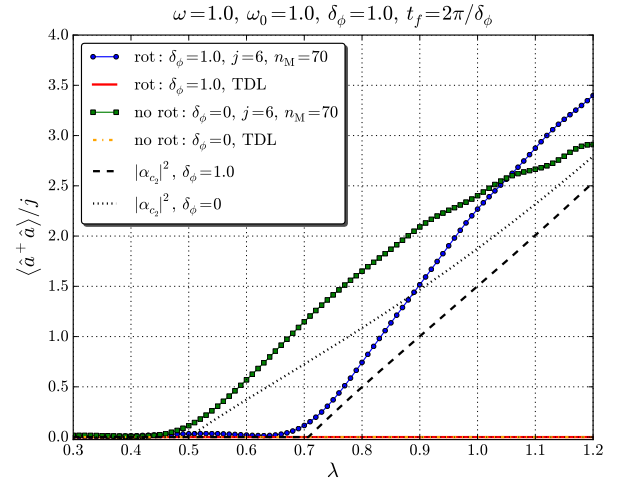


Figure 24: Scaled mean photon number dependence on the atom-field coupling strength on resonance $\omega = \omega_0 = 1.0$ for a rotation velocity $\delta_\phi = 1.0$. The system at $t_0 = 0$ is prepared in the state $|n=0\rangle|j, m=-j\rangle$.

ber becomes macroscopic for a coupling strength greater than some critical coupling. In the unrotated case this is given by $\lambda_c = \sqrt{\omega\omega_0}/2$ while for a rotational driving it is given by $\lambda_c^{(\text{rot})} = \sqrt{\omega(\omega_0 + \delta_\phi)}/2$. In the TDL the mean field solutions give zero.

By looking at the time evolution of the scaled mean photon number one can observe rather irregular structure of the oscillations. Motivated by this in Fig. (25) we also plot the time averaged scaled mean photon number as a function of λ for multiple rotations $t_f = 150 \cdot 2\pi/\delta_\phi$. This

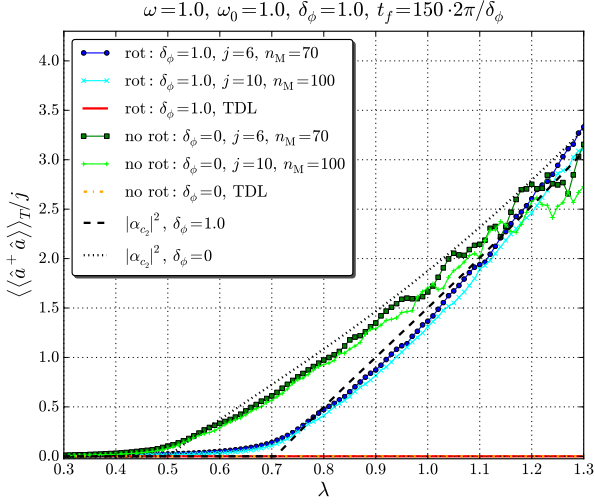


Figure 25: Time averaged scaled mean photon number on resonance $\omega = \omega_0 = 1.0$ for a rotation velocity $\delta_\phi = 1.0$. The system at $t_0 = 0$ is prepared in the state $|n=0\rangle|j, -j\rangle$ and evolved until $t_f = 150 \cdot 2\pi/\delta_\phi$. The mean field solutions in the TDL remain strictly zero.

plot shows that if we prepare the initial state to be a Fock state $|n=0\rangle|j, m=-j\rangle$ and evolve the system in time we observe two distinct phases. Below a critical coupling strength the time averaged scaled mean photon number is zero (normal phase) while above a critical coupling the time averaged scaled mean photon number becomes non-zero (super-radiant phase). Rotational driving shifts this critical coupling strength as $\lambda_c^{(\text{rot})} = \sqrt{\omega(\omega_0 + \delta_\phi)}/2$. We therefore conclude here that the evolution starting from this state is similar to the one corresponding to the initial state $|\alpha_{c_2}\rangle|\zeta_{c_2}\rangle$.

3. Dependence of the mean photon number on the rotation velocity δ_ϕ

Here we look into the dependence of the scaled mean photon number on the rotation velocity δ_ϕ , $\langle\langle \hat{a}^\dagger \hat{a} \rangle\rangle(\delta_\phi)/j$ when the system is initially prepared in the Fock state $|\psi(0)\rangle = |n=0\rangle|j, m=-j\rangle$. Again first, we consider only one rotation in the parameter space, $t_f = 2\pi/\delta_\phi$ and compare it to the undriven evolution (see Fig. 26).

We observe that if we encircle the critical paraboloid (\mathcal{C}_2)

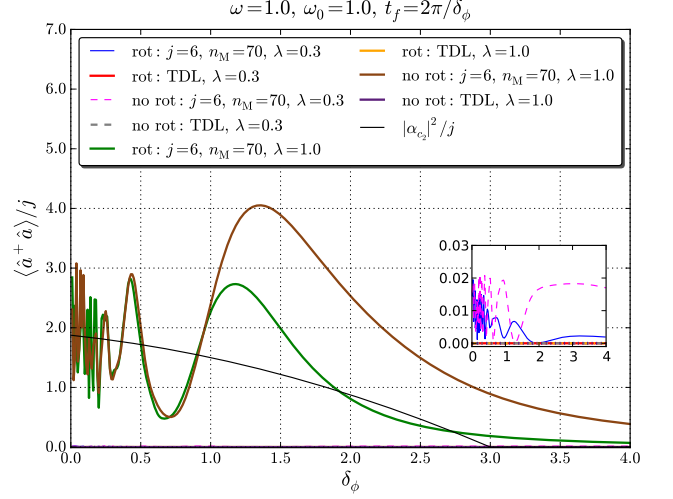


Figure 26: Dependence of $\langle\langle \hat{a}^\dagger \hat{a} \rangle\rangle_T / j$ on rotation velocity δ_ϕ after one circular evolution in the parameter space for a fixed atom-field coupling $\lambda = 1.0$. The mean field solution does not reproduce the finite size calculations it is strictly zero.

the scaled mean photon number shows velocity dependence. Fig. 27 shows the time averaged scaled mean photon number $\langle\langle \hat{a}^\dagger \hat{a} \rangle\rangle_T / j$ as a function of the rotation velocity δ_ϕ . It was averaged over a time interval of $t_f = 150 \cdot 2\pi/\delta_\phi$.

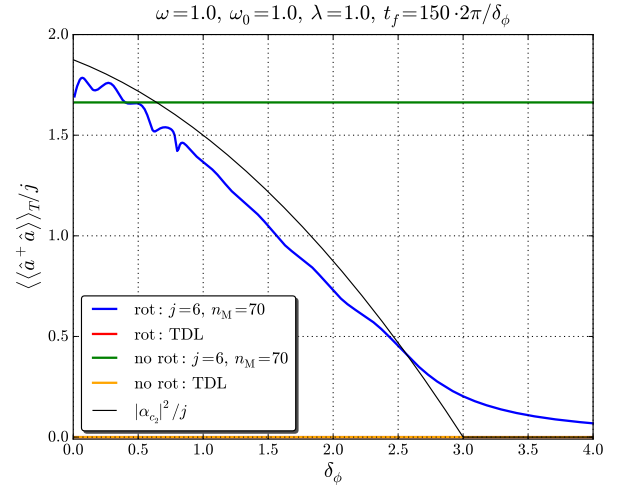


Figure 27: Dependence of the time averaged scaled mean photon number on the driving velocity at resonance $\omega = \omega_0 = 1.0$ and for $\lambda = 1.0$. At $t_i = 0$ the system is prepared in the state $|n=0\rangle|j, m=-j\rangle$ and evolved up to $t_f = 150 \cdot 2\pi/\delta_\phi$. The mean field solutions always stays zero.

It is clear that there is a critical driving velocity for rotational evolution given by $\delta_{\phi,c}^{(\text{rot})} = \frac{4\lambda^2}{\omega} - \omega_0$ allowing to probe two different non-equilibrium phases of the

Dicke model. On the other hand, in the case of the time evolution of the undriven Dicke Hamiltonian the time averaged scaled mean photon number becomes constant (if we encircle the critical paraboloid). This shows that the presence of the non-equilibrium transition in the Dicke model can depend on the initial state.

4. Parity $\hat{\Pi}$

Here we study the time evolution of the parity operator if the system is initially prepared in the Fock state. In Fig. 28 we show the time evolution of the parity operator $\langle \hat{\Pi} \rangle$ for different coupling strength at fixed finite spin $j = 10$. In this case the parity is always constant in time with no sign of change to zero at a critical coupling. The system always remains in the state with the same parity $+1$.

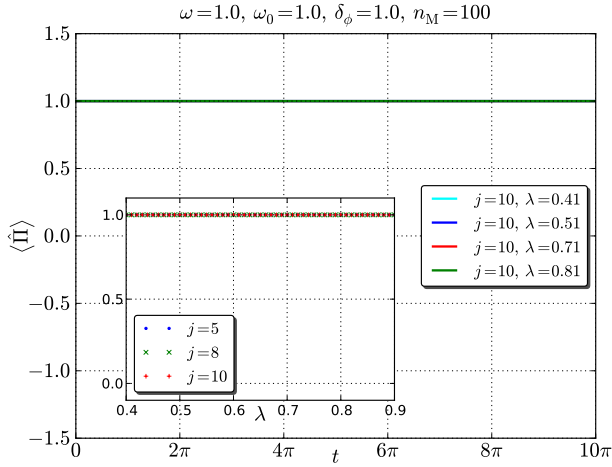


Figure 28: Time evolution of the parity operator when the system is driven from the initial Fock state $|n=0\rangle|j, m=-j\rangle$ for a pseudo spin of $j=10$. The inset shows the dependence on the atom-field coupling strength λ for different pseudo-spin length j .

In the TDL ($j \rightarrow \infty$) one can use the solutions of the mean field equations. In this case the parity is also unchanged (see Fig. 29) which can be traced back to the fact that the initial conditions $\alpha(0) = \alpha^*(0) = \zeta(0) = \zeta^*(0) = 0$ allow no quantum fluctuations and therefore do not evolve in time. Also in the case of the scaled phase space coordinates $(q_1, p_1, q_2, p_2) \rightarrow 1/\sqrt{j}(q_1, p_1, q_2, p_2)$ the parity is always $+1$.

E. Nearly Fock initial state:

$$|\alpha(0) = 10^{-\epsilon}\rangle|\zeta(0) = 10^{-\epsilon}\rangle$$

In the previous subsection we looked into the rotational dynamics of the Dicke model with the initial state given

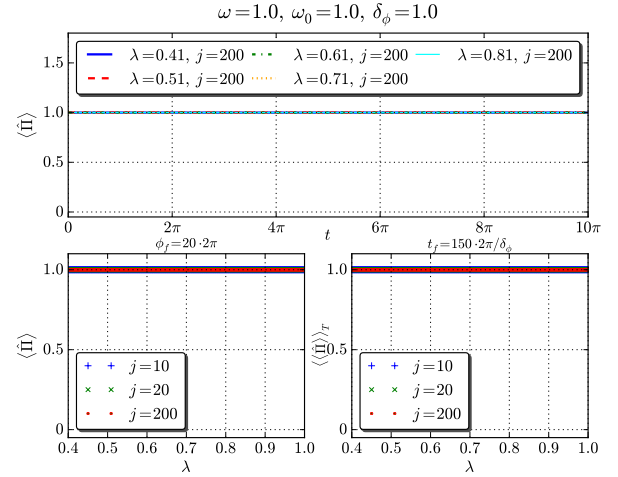


Figure 29: Upper panel: time evolution of the parity operator for the Fock initial state $|n=0\rangle|j, m=-j\rangle$. Lower left panel: dependence of the parity on the coupling constant λ after 20 circles. Lower right panel: dependence of the time averaged parity $\langle \langle \hat{\Pi} \rangle \rangle_T$ on the atom-field coupling λ .

by the Fock state with no photons $n=0$ and lowest weight spin state $m=-j$, $|\psi(0)\rangle = |n=0\rangle|j, m=-j\rangle$. This corresponds to zero parameters of the coherent states $\alpha=0$ and $\zeta=0$. This state does not evolve in time in the semi-classical limit. As shown in the previous paragraph the mean field equations did not reproduce the results calculated numerically for a system with a finite number of two-level atoms.

Motivated by this we study the effect of small perturbation of the initial conditions. We consider a situation when the parameters α and ζ are not strictly zero but small and parametrized as

$$\alpha(0) = 10^{-\epsilon}, \quad \zeta(0) = 10^{-\epsilon} \quad (94)$$

where ϵ is large. Consider the following initial coherent state

$$|\psi(t_0=0)\rangle = |\alpha(0) = 10^{-\epsilon}\rangle \otimes |\zeta(0) = 10^{-\epsilon}\rangle, \quad (95)$$

which differs slightly from the Fock state with no photons and lowest weight state: for example, for $j=10$ and $n_M=100$ we find for the overlap $\langle \alpha=10^{-3}, \zeta=10^{-3} | n=0, m=-j \rangle = 0.99999$.

We start the non-equilibrium evolution by switching on the rotation at $t_0=0$ and evolving the system until $t_f = n_R 2\pi/\delta_\phi$. Again we will compare the rotationally driven evolution and the free evolution.

1. Time evolution of the mean photon number

The time evolution of the scaled mean photon number, $\langle \hat{a}^\dagger \hat{a} \rangle / j$, is depicted in Fig. (30). It compares the scaled

mean photon number obtained for a finite system using the numerical Chebyshev scheme (blue and red curve) and the results of the TDL computed from the mean field equations (26)-(29) (green and orange curve). We

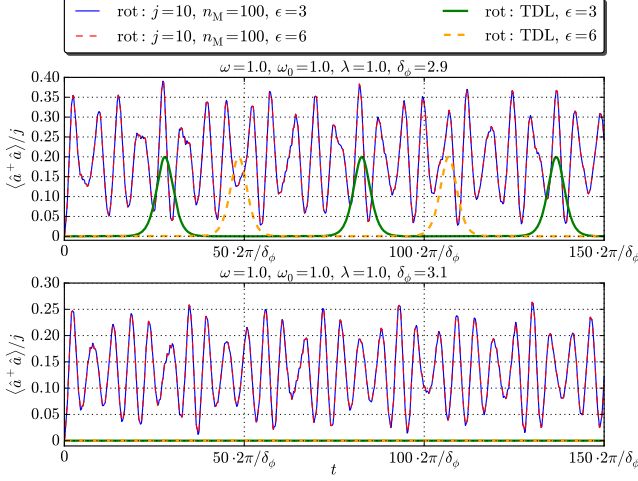


Figure 30: Time dependence of the scaled mean photon number on resonance $\omega = \omega_0 = 1.0$ and $\lambda = 1.0$ for two different rotations velocities: one is slightly below the critical driving velocity $\delta_{\phi,c} = 3.0$ while the second one is just above it. The system is initially prepared in the coherent state $|\alpha(0) = 10^{-\epsilon}\rangle|\zeta(0) = 10^{-\epsilon}\rangle$, with $\epsilon = 3$ and $\epsilon = 6$ for rotational driving.

observe that the initial state $|\alpha(0) = 10^{-\epsilon}\rangle|\zeta(0) = 10^{-\epsilon}\rangle$ for different ϵ does generate the same dynamics as the initial Fock state $|n=0\rangle|j, m=-j\rangle$ for a finite number of two-level atoms. However, in the TDL the mean field equations show macroscopic excitations if we encircle the criticality (here $\lambda = 1.0 > \lambda_c = 0.5$) and drive the system slower than the critical driving velocity $\delta_{\phi,c} = \frac{4\lambda^2}{\omega} - \omega_0$. We note that the “soliton train” appearing in this figure (green and yellow lines) is somewhat reminiscent to the findings of Ref. [15], [17]. Note however that the model we study here is non-integrable.

In Fig. (31) we show the time evolution of the scaled mean photon number with no rotational driving, i.e., the time evolution is governed by the usual Dicke Hamiltonian \hat{H}_D . Again, the system is initially prepared in the coherent state $|\alpha(0) = 10^{-\epsilon}\rangle|\zeta(0) = 10^{-\epsilon}\rangle$.

Summarizing these results we observe that the initial state $|\alpha(0) = 10^{-\epsilon}\rangle|\zeta(0) = 10^{-\epsilon}\rangle$ for different ϵ and finite j reproduces the same dynamics as for the initial Fock state $|n=0\rangle|j, m=-j\rangle$. In the TDL the mean field equations show a macroscopic excitations of the mean photon number in the super-radiant phase ($\lambda > \lambda_c$) if we use the initial conditions $\alpha(0) = \alpha^*(0) = \zeta(0) = \zeta^*(0) = 10^{-\epsilon}$. This means that small fluctuations present in the initial state make the quasi-classical description possible.

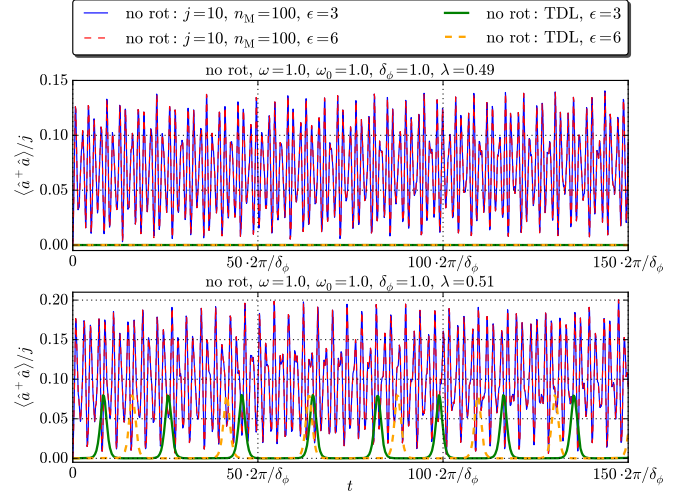


Figure 31: Time dependence of the scaled mean photon number on resonance $\omega = \omega_0 = 1.0$ for two different coupling strength λ : one slightly below the critical driving velocity $\lambda_c = \frac{\sqrt{\omega\omega_0}}{2} = 0.5$ and one just above it. The system is initially prepared in the coherent state $|\alpha(0) = 10^{-\epsilon}\rangle|\zeta(0) = 10^{-\epsilon}\rangle$, with $\epsilon = 3$ and $\epsilon = 6$ and evolved with undriven Hamiltonian.

2. Dependence of the mean photon number on the atom-field coupling strength λ

In Fig. 32 we plot $\langle\langle\hat{a}^\dagger\hat{a}\rangle\rangle_T/j$ as a function λ for the driven model (blue, red, green) and for the undriven one (cyan, orange, lime). We again observe a critical coupling strength λ_c at which the number of excited photons becomes macroscopic. In the case of rotational driving the critical coupling is shifted by the amount of the applied rotation velocity δ_ϕ . The λ -dependence of $\langle\langle\hat{a}^\dagger\hat{a}\rangle\rangle_T/j$ for the initial Fock state of the Dicke model with a finite number of atoms looks similar to the one obtained in the TDL with $\alpha(0) = \alpha^*(0) = \zeta(0) = \zeta^*(0) = 10^{-\epsilon}$. However, the main differences with a driven model are (i) appearance of dips and (ii) difference in the scaling form of the curve when $\lambda \rightarrow \lambda_c^{(\text{rot})}$.

3. Dependence of the mean photon number on the rotation velocity δ_ϕ

The dependence of $\langle\langle\hat{a}^\dagger\hat{a}\rangle\rangle_T/j$ on δ_ϕ for a driven (blue, red, green) and undriven (cyan, orange, lime) systems is shown in Fig. (33). When the critical paraboloid (path C_2) is encircled, there is a critical driving velocity given by $\delta_{\phi,c}^{(\text{rot})} = \frac{4\lambda^2}{\omega} - \omega_0$. This is in contrast to the TDL with the initial conditions $\alpha(0) = \alpha^*(0) = \zeta(0) = \zeta^*(0) = 0$ when the mean photon number was always zero. In the case of undriven model the time averaged scaled mean photon number fluctuates around a constant value.

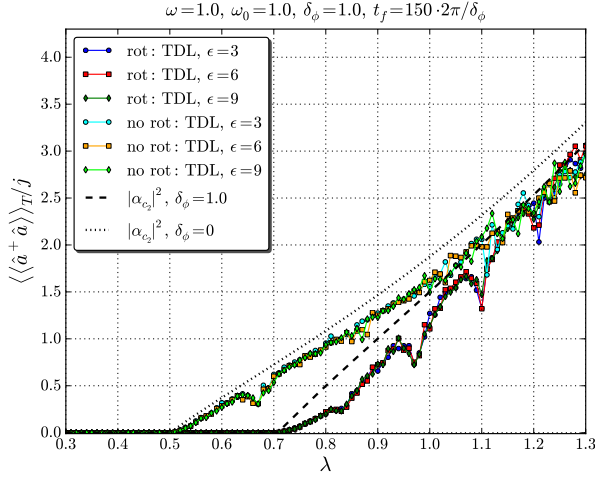


Figure 32: Time-averaged mean photon number $\langle\langle \hat{a}^\dagger \hat{a} \rangle\rangle_T / j$ as a function of the coupling strength. In the TDL ($j \rightarrow \infty$) obtained by solving the mean field equations (26)-(29) with the initial conditions $\alpha(0) = \alpha^*(0) = \zeta(0) = \zeta^*(0) = 10^{-\epsilon}$.

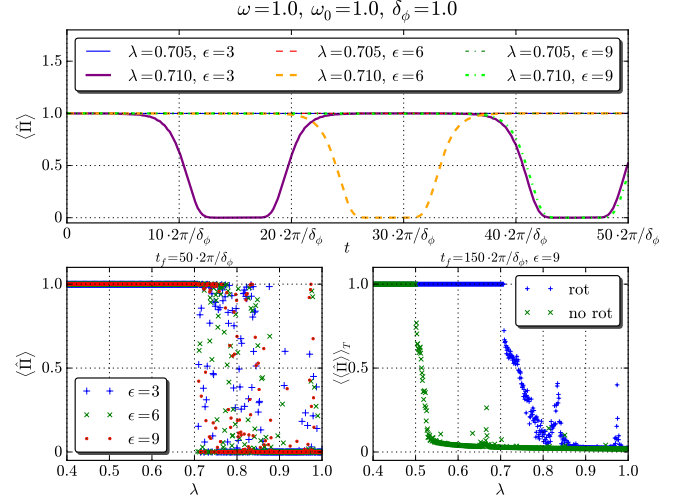


Figure 34: Upper panel: time evolution of the parity operator for the driven system starting from the nearly-Fock state. Lower left panel: the parity after 50 circles as a function of the coupling. Lower right plot: the same as left panel but averaged over 150 circles.

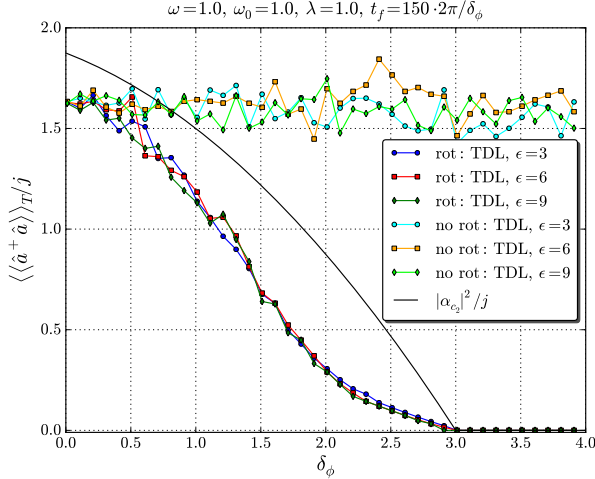


Figure 33: Time-averaged mean photon number $\langle\langle \hat{a}^\dagger \hat{a} \rangle\rangle_T / j$ as a function of the driving velocity. The TDL ($j \rightarrow \infty$) is obtained by solving the mean field equations (26)-(29) with the initial conditions $\alpha(0) = \alpha^*(0) = \zeta(0) = \zeta^*(0) = 10^{-\epsilon}$.

4. Parity $\hat{\Pi}$

Using the initial state $|\alpha(0) = 10^{-\epsilon}\rangle|\zeta(0) = 10^{-\epsilon}\rangle$ with $\epsilon > 2$ for a system of a finite number of atoms we find the same behavior, $\langle \hat{\Pi} \rangle = +1$, for any time and coupling strength as for the initial Fock state $|n=0\rangle|j, m=-j\rangle$. On the other hand, in the TDL ($j \rightarrow \infty$) using the solutions of the mean field equations (26)-(29) we compute the time evolution of the parity and observe (Fig. 34) that for a coupling $\lambda > \lambda_c^{(\text{rot})}$ the time evolution shows

a smooth jumps from +1 to 0. We also show the parity calculated using the rescaled phase space λ coordinates (see Fig. 35).

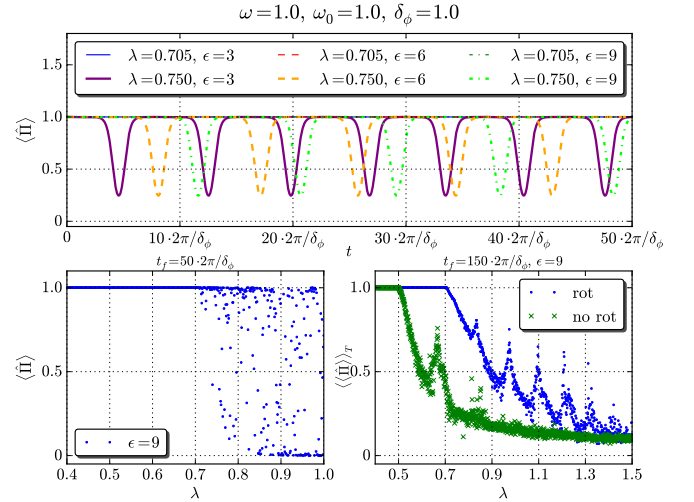


Figure 35: Upper panel: time evolution of the scaled parity operator when we start the rotational dynamics with the system prepared in the nearly-Fock state. Lower left panel: the scaled parity as a function of λ after 50 circles. Lower right panel: the same as the left one but averaged over 150 circles.

F. Ground state of the un-rotated Dicke model as initial state: $|\text{GS}\rangle$

Here we consider the evolution of a system initially prepared in the ground state

$$|\psi(t_0 = 0)\rangle = |\text{GS}\rangle. \quad (96)$$

First, we numerically compute the ground state $|\text{GS}\rangle$ of the Dicke Hamiltonian \hat{H}_D by truncating the bosonic Hilbert space up to n_M while maintaining the full Hilbert space of the pseudo-spin j . Then, at $t_0 = 0$, we start to evolve the system according to the rotated Dicke model $\hat{H}_{RD}(t)$. Next we measure the scaled mean photon number $\langle \hat{a}^\dagger \hat{a} \rangle$ as

$$\begin{aligned} \langle \hat{a}^\dagger \hat{a} \rangle &= \langle \psi(t_f) | \hat{a}^\dagger \hat{a} | \psi(t_f) \rangle \\ &= \langle \text{GS} | e^{i\hat{H}_{RD}t_f} \hat{a}^\dagger \hat{a} e^{-i\hat{H}_{RD}t_f} | \text{GS} \rangle, \end{aligned} \quad (97)$$

where the final time is, as before, given by $t_f = n_R 2\pi/\delta_\phi$. We also consider the undriven evolution governed by the evolution of the usual Dicke model \hat{H}_D .

1. Time evolution of the mean photon number

The time dependence of the scaled mean photon number is shown in Fig. 36. Here we compare the results for the initial ground state $|\text{GS}\rangle$ (red curves) with the results for the initial coherent state with the parameters α_{cst} and ζ_{cst} (blue and green curves). The dashed lines show the situation for the undriven evolution.

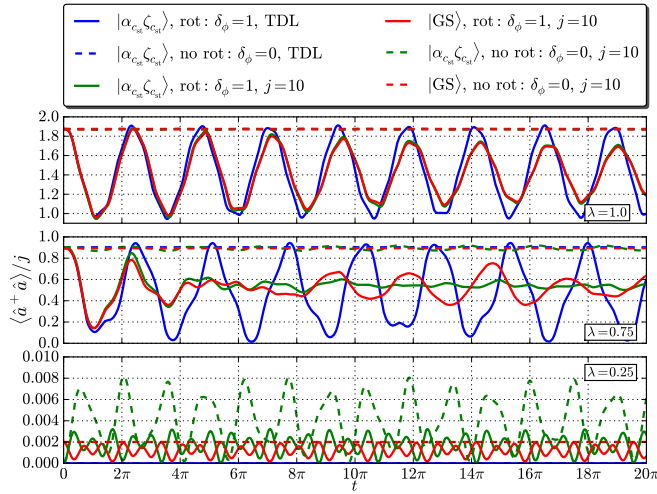


Figure 36: Time dependence of the scaled mean photon number on resonance $\omega = \omega_0 = 1.0$ for different values of the coupling strength λ . Here we compare the results for different initial states: $|\text{GS}\rangle$ and $|\alpha_{cst}\rangle|\zeta_{cst}\rangle$. The ground state $|\text{GS}\rangle$ is obtained numerically and we choose $n_M = 100$.

For the rotationally driven case (solid lines) we observe an oscillatory behavior of the scaled mean photon num-

ber. For a finite number of atoms the time evolution of the scaled mean photon number for the ground state $|\text{GS}\rangle$ is close to the one for the coherent state $|\alpha_{cst}\rangle|\zeta_{cst}\rangle$. For large atom-field couplings they become identical. Thus, the coherent state $|\alpha_{cst}\rangle|\zeta_{cst}\rangle$ is a good approximation for the ground state of the system even in the driven case. This phenomenon is noticed already in [22]. In the undriven case the time evolution of the mean photon number for the ground state is constant and corresponds to the value found in the TDL

$$\langle \text{GS} | \hat{a}^\dagger \hat{a} | \text{GS} \rangle = \begin{cases} \frac{1}{2} \left(\frac{2\lambda}{\omega} \right)^2 \left[1 - \left(\frac{\omega\omega_0}{4\lambda^2} \right)^2 \right] & \text{if } \lambda \geq \frac{1}{2} \sqrt{\omega\omega_0} \\ 0 & \text{if } \lambda < \frac{1}{2} \sqrt{\omega\omega_0} \end{cases}. \quad (98)$$

2. Dependence of the mean photon number on the atom-field coupling strength λ

Here we study the dependence of the scaled mean photon number on the atom-field coupling strength λ . First, we consider one revolution in parameter space, $t_f = 2\pi/\delta_\phi$. This case is shown for a fixed rotation velocity $\delta_\phi = 1.0$ at resonance $\omega = \omega_0 = 1.0$, in Fig. 37. We also show the dependence of the scaled mean photon number on λ for the undriven Dicke model (green curve), where the final time was kept the same $t_f = 2\pi/\delta_\phi$.

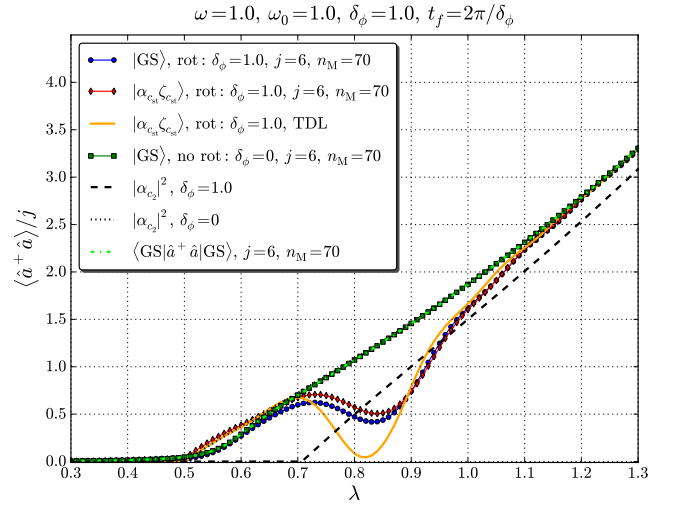


Figure 37: The scaled mean photon number as a function of the atom-field coupling strength: here we compare the mean field solution ($j \rightarrow \infty$) for the initial coherent state $|\alpha_{cst}\rangle|\zeta_{cst}\rangle$ (yellow solid line) with the time evolution calculated numerically for a system with a finite number of atoms ($j = 6$) for the initial state chosen as ground state $|\text{GS}\rangle$ (blue line) and the coherent state (red line). We also compare it with the undriven case (green line) and the static (dashed line).

As we have already seen the time dependence of the scaled mean photon number calculated for the initial ground state $|\text{GS}\rangle$ and for the initial coherent state

$|\alpha_{c_{st}}\rangle|\zeta_{c_{st}}\rangle$ give qualitatively the same results. For the ground initial state we observe a minimum in the super-radiant phase (in Fig. 37 at $\lambda \approx 0.82$). This indicates a competition between the two stationary states or the ground states of the rotationally driven and undriven Dicke Hamiltonians. One further interesting point is the difference in scaling behavior close to the critical point $\lambda_c = \sqrt{\omega\omega_0}/2$: This behavior is different for the initial ground and coherent states. For the ground state it follows the same scaling behavior as in the static and unrotated case.

So far we considered the mean photon number after one circle $\phi_f = 2\pi$, but the situation with many rotations $\phi_f \rightarrow \infty$ represent an interesting limit. In this case the interplay of dynamical and geometrical phase may be a source some new effects [14]. Considering the case of many rotations in Fig. 36 it is natural to take the time average of the scaled mean photon number as already defined in Eq. (81). The time averaged scaled mean photon number $\langle\langle\hat{a}^\dagger\hat{a}\rangle\rangle_T/j$ is depicted in Fig. 38. Here we averaged over a time interval of $t_f = 150 \cdot 2\pi/\delta_\phi$ for the resonance conditions $\omega = \omega_0 = 1.0$ and kept the rotation velocity to be $\delta_\phi = 1.0$.

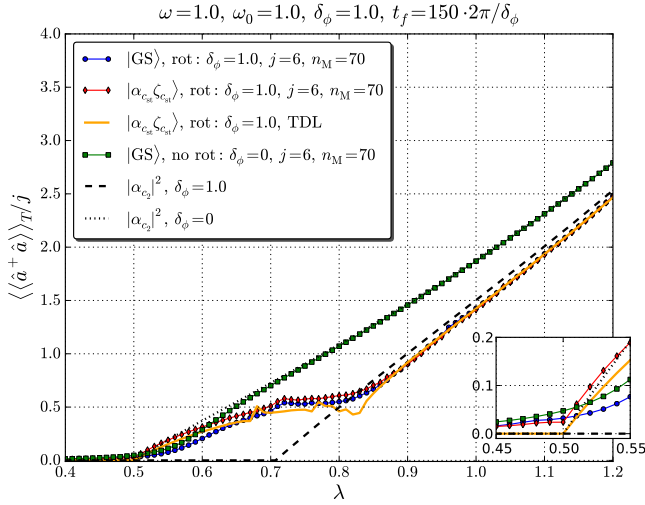


Figure 38: The time averaged scaled mean photon number $\langle\langle\hat{a}^\dagger\hat{a}\rangle\rangle_T/j$ at resonance $\omega = \omega_0 = 1.0$ as a function of the coupling λ . The system is initially prepared in the ground state $|\text{GS}\rangle$ which is calculated numerically and then evolved until $t_f = 150 \cdot 2\pi/\delta_\phi$ (blue curve). The result is compared with the one obtained for the initial coherent state (red and yellow curve) and with the one corresponding to undriven system (green line).

We qualitatively observe the same behavior for the time averaged scaled mean photon number for the two different initial states, namely for the ground state $|\text{GS}\rangle$ and for the coherent state $|\alpha_{c_{st}}\rangle|\zeta_{c_{st}}\rangle$. Moreover, the time averaged scaled mean photon number shows a different scaling for the two initial states when approaching the equilibrium critical coupling $\lambda_c = \sqrt{\omega\omega_0}/2$.

3. Dependence of the mean photon number on the rotation velocity δ_ϕ

In this subsection we illustrate the dependence of the scaled mean photon number on the rotation velocity δ_ϕ . First, in Fig. 39 we consider one revolution, $t_f = 2\pi/\delta_\phi$ for different atom-field couplings and for $\omega = \omega_0 = 1.0$. We plot the velocity dependence of the scaled mean photon number for rotational driving once for the initial ground state $|\text{GS}\rangle$ (solid blue and solid green curve) and for the initial coherent state $|\alpha_{c_{st}}\rangle|\zeta_{c_{st}}\rangle$ (dashed blue and green curves and solid red and orange curves). We also show the undriven situation (pink and cyan) and the static (brown dashed curve). The behavior of $\langle\hat{a}^\dagger\hat{a}\rangle/j$

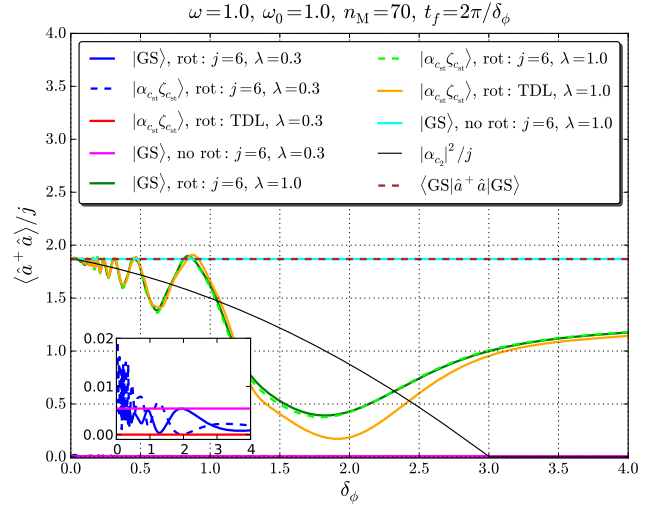


Figure 39: The scaled mean photon number on a resonance $\omega = \omega_0 = 1.0$ for $\lambda = 0.3$ and $\lambda = 1.0$ as a function of the driving velocity. We compare $\langle\hat{a}^\dagger\hat{a}\rangle(t_f, \delta_\phi)/j$ for two different initial states: $|\text{GS}\rangle$ and $|\alpha_{c_{st}}\rangle|\zeta_{c_{st}}\rangle$ for the driven and undriven situation (with $t_f = 2\pi/\delta_\phi$ in both cases).

for the two different initial state $|\text{GS}\rangle$ and $|\alpha_{c_{st}}\rangle|\zeta_{c_{st}}\rangle$ is qualitatively similar. Namely that if the equilibrium critical paraboloid is not encircled $\lambda < \lambda_c = \sqrt{\omega\omega_0}/2$ then the mean photon number is zero. But if we encircle it ($\lambda > \lambda_c = \sqrt{\omega\omega_0}/2$) the mean photon number becomes macroscopic. There is no critical driving velocity in the driven case. We remind that for the stationary state of the rotated Dicke model (see black curve in Fig. 39) $\delta_{\phi,c}^{(\text{rot})} = \frac{4\lambda^2}{\omega} - \omega_0$.

Next in Fig. 40 we consider $\langle\langle\hat{a}^\dagger\hat{a}\rangle\rangle_T/j$ as a function of δ_ϕ averaged over a time span of $t_f = 150 \cdot 2\pi/\delta_\phi$ at resonance $\omega = \omega_0 = 1.0$ for the protocol which encircles the equilibrium critical paraboloid $\lambda = 1.0$. We show $\langle\langle\hat{a}^\dagger\hat{a}\rangle\rangle_T/j$ for the two initial states $|\text{GS}\rangle$ and $|\alpha_{c_{st}}\rangle|\zeta_{c_{st}}\rangle$. Also we compare the driven and undriven situations.

To summarize, we see that the dynamics of the mean photon number for the initial ground state $|\text{GS}\rangle$ and for the initial coherent state $|\alpha_{c_{st}}\rangle|\zeta_{c_{st}}\rangle$ are very similar. Evo-

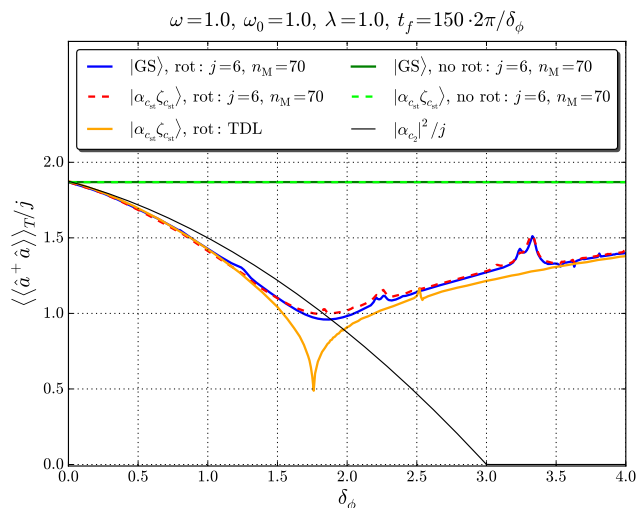


Figure 40: The time averaged scaled mean photon number on resonance $\omega = \omega_0 = 1.0$ for $\lambda = 1.0$ as a function of the driving velocity. We plot $\langle \hat{a}^\dagger \hat{a} \rangle(t_f, \delta_\phi)/j$ for two different initial states: $|\text{GS}\rangle$ and $|\alpha_{c_{\text{st}}}\rangle|\zeta_{c_{\text{st}}}\rangle$ for the driven and undriven situations (with $t_f = 150 \cdot 2\pi/\delta_\phi$ in both cases).

lution starting from these initial states for a finite number of atoms has a tendency to develop two new sub-phases in the super radiant phase. Similarly, evolution from both states develops a new dynamical critical coupling $\lambda_c^{(\text{dyn})}$ or critical driving velocity $\delta_{\phi,c}^{(\text{dyn})}$ in the thermodynamic limit. This phenomenon is traced back to the interplay of geometric and dynamical phases in dynamics. Finally, we remark that the non-equilibrium phase diagram for the initial coherent state $|\alpha_{c_{\text{st}}}\rangle|\zeta_{c_{\text{st}}}\rangle$ is the same as for the initial ground state $|\text{GS}\rangle$.

4. Parity $\hat{\Pi}$

Here we illustrate the time evolution of the parity operator $\langle \psi(t) | \hat{\Pi} | \psi(t) \rangle$. The result, for a situation when the initial state is the ground state of the unrotated Dicke model, $|\text{GS}\rangle$, while the evolution is given by $\hat{H}_{\text{RD}}(t)$, is shown in Fig. 41. The calculation was done numerically according to the Chebyshev scheme for a finite number of atoms j .

One can clearly see that the parity is always constant in time. More interesting is that there is no transition to zero, at a critical coupling. Apparently the system always remains in the state with the same parity equal to +1.

V. CONCLUSION

In conclusion, we studied the dynamics of the rotationally driven Dicke model beyond the rotating wave

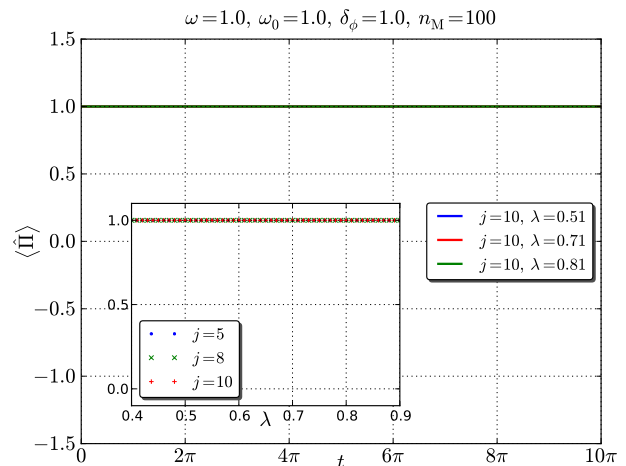


Figure 41: Time evolution of the parity operator when the dynamics is started from the ground state of the unrotated Dicke model $|\text{GS}\rangle$. The inset plot shows the dependence on the atom-file coupling strength λ for different pseudo-spin length j .

approximation. We calculated the time evolution of the mean photon number and the expectation values of the parity operator of the system for different initial states: (i) stationary Dicke coherent state $|\alpha_{c_{\text{st}}}\rangle|\zeta_{c_{\text{st}}}\rangle$, (ii) the stationary coherent state $|\alpha_{c_2}\rangle|\zeta_{c_2}\rangle$ of the rotated Dicke model $\hat{H}_{\text{RD}}(t)$, (iii) Fock state $|n=0\rangle|j, m=-j\rangle$ and (iv) the ground state $|\text{GS}\rangle$ of the Dicke model. In order to understand the influence of the geometric phase on the non-equilibrium dynamics we compared the time evolution for the rotationally driven Dicke model $\hat{H}_{\text{RD}}(t)$ and the evolution of the Dicke model \hat{H}_{D} without driving.

Here is the summary of our findings for different physically relevant initial states. (i) For the stationary Dicke initial state (stationary state of the usual Dicke model \hat{H}_{D}) we observe in the TDL a reentrant meta stable phase in the super-radiant phase. This is clearly manifested in the time averaged scaled mean photon number. We observe that the system developed a dynamical critical coupling strength $\lambda_c^{(\text{dyn})}$ and dynamical critical driving velocity $\delta_{\phi,c}^{(\text{dyn})}$. Dynamical quantum phase transition is identified as a sudden change in the dynamical behavior of observables as a function of the driving parameters in real time. We suggest that this critical behavior results from a competition of the geometric phase and the dynamical phase which can give rise to a resonance phenomenon described in Ref. [14]. By looking at the time averaged scaled mean photon number we constructed a non-equilibrium phase diagram. The time evolution of the parity operator reveals a similar phenomenon of appearance of a meta stable phase and provides a complementary information about a new metastable phase. Further, we observe that this type of non-equilibrium driving

allows one to probe the equilibrium quantum criticalities “from a distance” in parameter space, namely by encircling a quantum critical surface in parameter space without actual crossing it. This may provide a useful experimental hint since the quantum state will not be destroyed by crossing the quantum critical point.

(ii) For the stationary circle initial state $|\alpha_{c_2}\rangle|\zeta_{c_2}\rangle$ (stationary coherent state of the rotated Dicke model \hat{H}_{RD}) we found a shift in the critical coupling by the amount given by the applied rotation velocity $\lambda_c^{(\text{rot})} = \sqrt{\omega(\omega_0 + \delta_\phi)}/2$. This defines a critical rotation driving velocity $\delta_{\phi,c}^{(\text{rot})} = \frac{4\lambda^2}{\omega} - \omega_0$. Which can otherwise be understood by making a transformation into a rotating frame and considering the effective Hamiltonian \hat{H}_{ROT} in this basis. The expectation value of the parity operator shows a constant time evolution and goes to zero at the critical coupling $\lambda_c^{(\text{rot})}$.

(iii) For the Fock state with no photons and lowest spin projection $|n=0\rangle|j,-j\rangle$ we obtain, for a finite number of atoms, a mean photon number which is different from zero. We observe the same rotational critical coupling $\lambda_c^{(\text{rot})} = \sqrt{\omega(\omega_0 + \delta_\phi)}/2$ in this case and therefore $\delta_{\phi,c}^{(\text{rot})} = \frac{4\lambda^2}{\omega} - \omega_0$, the same as for the initial state $|\alpha_{c_2}\rangle|\zeta_{c_2}\rangle$. The mean field solution does not evolve in time and produces trivial results if we choose the parameters of the initial conditions as $\alpha_0 = \alpha_0^* = \zeta_0 = \zeta_0^* = 0$. However, calculations for a very small initial value of the parameters (which can be interpreted as quantum

fluctuations) $\alpha_0 = \alpha_0^* = \zeta_0 = \zeta_0^* = 10^{-\epsilon}$ reveal a non zero mean photon number in the TDL using the mean field equations. For the time averaged quantities we also observe the same rotational critical coupling $\lambda_c^{(\text{rot})} = \sqrt{\omega(\omega_0 + \delta_\phi)}/2$ and $\delta_{\phi,c}^{(\text{rot})} = \frac{4\lambda^2}{\omega} - \omega_0$, as before. The parity is always constant and equals one for a finite number of two-level atoms which also holds in the TDL. On the other hand, for small non-zero initial conditions we observe an oscillatory behavior of the parity expectation value.

(iv) For the initial state given by the ground state |GS) (which is computed numerically by diagonalizing the Dicke Hamiltonian \hat{H}_D) we observe the same dynamical behavior as for the stationary Dicke state $|\alpha_{c_{st}}\rangle|\zeta_{c_{st}}\rangle$. This shows that these two states become equivalent in the TDL.

Summarizing, non-equilibrium dynamics of the Dicke model shows several universal properties independent on the precise nature of the initial state and exhibits interesting non-equilibrium quantum critical behavior which can be traced back to a competition of geometric and dynamical phases.

VI. ACKNOWLEDGMENTS

This work is supported by Swiss National Science Foundation. V.G. is grateful to KITP for hospitality.

-
- [1] R.H. Dicke, Phys. Rev. **93**, 99 (1954).
 - [2] M. Tavis and F. W. Cummings, Phys. Rev. **170**, 379 (1968); M. Tavis, arXiv:1206.0078.
 - [3] K. Hepp and E. H. Lieb, Ann. Phys. **76**, 360 (1973).
 - [4] Y. K. Wang and F. T. Hioe, Phys. Rev. A **7**, 831 (1973).
 - [5] H. J. Carmichael, C. W. Gardiner, and D. F. Walls, Phys. Lett. A **46**, 47 (1973).
 - [6] K. Rzazewski, K. Wódkiewicz, and W. Zakowicz, Phys. Rev. Lett. **35**, 432 (1975).
 - [7] J. Keeling, J. Phys.: Cond. Mat. **19**, 295213 (2007).
 - [8] A. Vukics, P. Domokos, arXiv:1206.0752.
 - [9] F. Brennecke, T. Donner, S. Ritter, T. Bourdel, M. Köhl, and T. Esslinger, Nature **450**, 268 (2007).
 - [10] A. Altland, V. Gurarie, T. Kriecherbauer, A. Polkovnikov, Phys. Rev. A **79**, 042703 (2009).
 - [11] A.P. Itin, P. Törmä, Phys. Rev. A **79**, 055602 (2009); arXiv:0901.4778.
 - [12] A. Altland, F. Haake, Phys. Rev. Lett. **108**, 073601 (2012); arXiv:1201.6514.
 - [13] V. M. Bastidas, C. Emary, B. Regler, T. Brandes, Phys. Rev. Lett. **108**, 043003 (2012).
 - [14] M. Tomka, A. Polkovnikov, V. Gritsev, Phys. Rev. Lett. **108**, 080404 (2012).
 - [15] E. A. Yuzbashyan, V. B. Kuznetsov, and B. L. Altshuler, Phys. Rev. B **72**, 144524 (2005); E. A. Yuzbashyan, O. Tsypliyatyev, and B. L. Altshuler, Phys. Rev. Lett. **96**, 097005 (2006).
 - [16] O. Tsypliyatyev and D. Loss, Phys. Rev. B **82**, 024305 (2010); O. Tsypliyatyev and D. Loss, Phys. Rev. A **80**, 023803 (2009).
 - [17] Ch. Sträter, O. Tsypliyatyev, A. Faribault, arXiv:1209.0292.
 - [18] C. Emary and T. Brandes, Phys. Rev. E **67**, 066203 (2003).
 - [19] F. Plastina, G. Liberti and A. Carollo, Europhys. Lett., **76**, 182 (2006).
 - [20] G. Chen, J. Li and J.-Q. Liang, Phys. Rev. A **74**, 054101 (2006).
 - [21] W. Zhang, D.H. Feng and R. Gilmore, Rev. Mod. Phys. **62**, 867 (1990).
 - [22] R. Gilmore, Catastrophe Theory for Scientists and Engineers (Dover Publications, New York, 1993)
 - [23] M. J. Bhaseen, J. Mayoh, B. D. Simons, and J. Keeling, Phys. Rev. A **85**, 013817 (2012).
 - [24] H. Tal-Ezer and R. Kosloff, J. Chem. Phys. **81**, 3967 (1984).